On the Rate-dependency of Mechanical Properties and Failure Mechanisms of a ($\gamma + \alpha_2$) - TiAl/Ti_3Al-Al_2O_3 Cermet

Haoyang Li[a, *], Pouyan Motamedi[a, b], James David Hogan[a]

[a] *Department of Mechanical Engineering, The University of Alberta, Edmonton, AB T6G 2R3, Canada*
[b] *Nanotechnology Research Centre, National Research Council Canada, 11421 Saskatchewan Dr., Edmonton, AB T6G 2R3, Canada*

Abstract

This study investigated the rate-dependent mechanical properties and failure of a self-propagating high-temperature synthesized TiAl/Ti_3Al-Al_2O_3 cermet using mechanical testing and advanced microscopy. Quasi-static and dynamic uniaxial compression tests coupled with high-speed imaging and digital image correlation were used to determine the rate-dependency of stress-strain behavior, compressive strength, and failure strain. The stress-strain curves in the dynamic experiments exhibited a series of alternating stress relaxation and strain hardening cycles, where a 1.3 times increase in compressive strength from 2780 ± 60 MPa to 3410 ± 247 MPa, and a 1.4 times increase in failure strain from 0.0166 ± 0.0017 to 0.0264 ± 0.0032 were determined with a seven order increase in strain rates from ~ 10^{-4} s^{-1} to ~ 10^{3} s^{-1}. It was also found that the cermet exhibits macroscopic surface texturing by examining the high-speed imaging of deformation during testing. Advanced microscopy, including scanning electron microscopy, high-resolution transmission electron microscopy, and two-dimensional x-ray diffraction were used to map out the failure mechanisms activated under the different loading rates. Globally distributed dislocations and twinning were observed as a consequence of dynamic loading, and extensive cleavage in the titanium aluminide phase, void growth, transgranular cracking, and particle fracture were

* Corresponding author
Email addresses: haoyang@ualberta.ca (HY. Li), p.motamedi@ualberta.ca (P. Motamedi) jdhogan@ualberta.ca (J.D. Hogan).

identified as the dominant failure mechanisms activated under the high strain rate loading. Crystalline texturing with profound microstructural evolution in the titanium aluminide phase was also found under dynamic loading, and this was correlated with the macroscopic surface texturing observed using high-speed imaging and the cyclical stress relaxation and strain hardening behavior in the stress-strain curves. This study presents a thorough understanding of the rate-dependency of the TiAl/Ti_3Al-Al_2O_3 cermet and provides insights in cermet material micromechanical modeling and improvement.

Keywords: cermet; two-phase titanium aluminide; quasi-static and dynamic uniaxial compression tests; rate-dependency; compressive strength; stress-strain response; failure mechanisms; crystalline texturing; microstructural evolution; digital image correlation

---

* Corresponding author
Email addresses: haoyang@ualberta.ca (HY. Li), p.motamedi@ualberta.ca (P. Motamedi) jdhogan@ualberta.ca (J.D. Hogan).

1. Introduction

The mechanical properties of metal matrix composites (MMCs) and their performance under various loadings have been extensively studied (e.g., indentation [1], compression [2], tension [3], ballistic [4], and shock [5]). After the term "hardmetal" was introduced by Schwarzkopf and Kieffer in 1953 [6], research on how to combine ceramics and metallic alloys in order to improve their performance over their consitiuents has been occuring ever since. The term "cermet" was introduced in the 1960s to designate a material made of the combination of ceramics and metallic alloys, including "hardmetal". The main motivation behind research on cermets has been to add the ductility of metals while preserving ceramic-like properties, such as high hardness and stiffness [4]. Early studies on cermets focused on manufacturing cutting tools by incorporating metallic alloys into systems like titanium carbide (TiC), tungsten carbide (WC), and titanium carbonitride (TiCN) [7, 8]. Mechanical properties of various cermet systems, including the SiC-Al system [9], TiC-Ni system [10], and WC-Co system [11], have been emphasized for applications such as body armors [12], turbine blades [13], and coating for cutting blades [13], where the first two require high strength-to-weight ratio and the third requires high hardness.

Much of the published literature on cermets is dedicated to the characterization of quasi-static mechanical properties and their relation to composition and microstructure [14 – 16]. Recently, other forms of cermets have gained interest for applications in extreme environments, such as high temperature and high loading rates. For example, Rittel et al. [17] investigated the high-rate mechanical behavior of a TiC-1080 steel cermet, and Ramesh and Ravichandran [18] studied the dynamic behavior of B_4C-Al cermet. However, little information is available on the rate-dependent behavior and fracture mechanisms of oxide cermets even though they have gained interests for defense and wear applications [8]. This is likely a consequence of the poor wettability between

oxide-type ceramics (e.g., Al_2O_3 and ZrO_2) and metals using conventional fabrication methods. This accompany with challenges in manufacturing and, thus, studying them dynamically. The poor wettability of oxide cermets leads to a reduction in toughening effects by the metallic phase [8], a counterproductive effect in cermet development. The dynamic behavior of the oxide-based cermets is nevertheless of primary importance since the mechanical and fracture responses are essential for understanding the material, as well as improving their usage in impact or other high-pressure applications [19].

Among promising oxide-based cermets for protection applications is the $TiAl/Ti_3Al$-Al_2O_3 cermet. The two phase titanium aluminide alloys, including the γ-TiAl and α_2-Ti_3Al phases, have attracted attention in recent decades because of their low density (3.7 – 4.7 g/cm^3), high melting temperature (~ 1500 °C), and good combination of stiffness (~ 180 GPa), specific strength (100 – 150 MPa/gcm^{-3}), and toughness (11 – 20 MPa$\sqrt{m}$) [20 – 23]. In addition, alumina (Al_2O_3) with its adequately low density (~ 3.9 g/cm^3) and moderate strength in the family of advanced ceramics (e.g., stiffness of 370 GPa and compressive strength of 2600 MPa for alumina AD995 reported by Coorstek. Inc. [24]), is still one of the preferred candidates for some protection applications in defense due to its low cost and availability [25]. With the advancement in manufacturing techniques such as reaction synthesis (RS) and spark plasma sintering (SPS), combining the titanium aluminide alloys with alumina to form a cermet seems promising due to their comparable densities (~ 3.9 g/cm^3) and coefficients of thermal expansion (~ 8.2 x 10^{-6} /°C for alumina [24] and ~ 8.5 x 10^{-6} /°C for titanium aluminide [26] at room temperature). One such fabrication method includes the self-propagation high-temperature sintering technique used in the present study to fabricate the $TiAl/Ti_3Al$-Al_2O_3 cermet, which has been noted by Levashov et al. [27] to yield better interface bonding between the matrix and the particles by direct phase forming from chemical

reactions. To date, literature published on the TiAl/Ti_3Al-Al_2O_3 cermet has focused primarily on novel manufacturing processes and powder mixture formulations, with limited experimentation studies on their rate-dependent mechanical properties and fracture mechanisms [28 – 32]. For example, Shen et al. [33] reported the quasi-static fracture toughness of a TiAl/Ti_3Al-Al_2O_3 cermet as a complementary part to discuss the quality of fabrication, while Lapin et al. [34] discussed the effect of the size and volume percentage of the alumina particles on the Vickers hardness and room-temperature quasi-static compression properties of a directionally-solidified titanium aluminide alloy. The limited information on high-rate properties of TiAl/Ti_3Al-Al_2O_3 cermets will need to be addressed before the material can be further utilized for commercial applications in, for example, body armors and turbine blades, where high velocity impacts are prevalent.

To address the gap in evaluation and understanding of the rate-dependent material properties and failure behavior, the current study explores the stress-strain responses of a self-propagating high-temperature synthesized TiAl/Ti_3Al-Al_2O_3 cermet under quasi-static and dynamic compressive loading rates. Novel digital image correlation (DIC) techniques coupled with high speed imaging is used to extract the strain field during testing. The rate-dependency of mechanical properties and fracture mechanisms are observed and discussed further by using mechanical testing and microscopic diagnostic. Scanning electron microscopy (SEM) and high-resolution (scanning) transmission election microscopy (HR-TEM/STEM) are used to probe the micro and nano-scale deformation mechanisms activated under the quasi-static and dynamic loading rates. Possible phase transformation and crystalline texturing are also investigated through the use of two-dimensional x-ray diffraction (2D-XRD). In the discussion, length scale-dependent failure mechanism observed using high speed imaging and advanced microscopy are linked with rate-dependent stress-strain behavior (i.e., stiffness, the stress relaxation and strain hardening

phenomena, peak stresses, and failure strains). From there, we compare these behaviors with those observed in other advanced ceramics and cermet systems. Lastly, this study concludes with discussion of implications for ballistic applications in the context of the new understanding on rate-dependent properties and mechanisms in this cermet system.

2. Material microstructure and preparation

2.1 As-received material microstructure

Multiple approaches can be used to fabricate the TiAl/Ti_3Al-Al_2O_3 cermet, including mechanical alloying [32] and reaction sintering [35]. Different fabrication methods produce vastly different microstructures [36, 37], where these microstructures have effects on the material performance. For example, Travitzky et al. [37] produced an interpenetrating phase morphology of a TiAl/Al_2O_3 cermet synthesized by thermal explosion with a continuous alumina network (grain size ~ 3 μm). In the Travitzky et al. [37] study, the material had a fracture toughness of 7.1 MPa $\sqrt{m}$. In a separate approach, Forouzanmehr et al. [32] obtained a nanograined TiAl/α-Al_2O_3 cermet (~ 58 nm grain size for TiAl and ~ 50 nm for Al_2O_3) via mechanical alloying. In the current study, the TiAl/Ti_3Al-Al_2O_3 cermet is manufactured by Luminant Corporation, British Columbia, and it is fabricated through the self-propagation high-temperature sintering (SHS), which is a highly exothermic reaction process under high pressures and temperatures. Figure 1-a presents a backscattered FESEM micrograph of the polished surface of the as-received material in this study. The micrograph is obtained using a Zeiss Sigma FESEM machine. An ultrafine but heterogeneous microstructure is formed in the cermet, and the alumina phase (darker regions) appears as a cluster network in the material, as was the case in Huy et al. [133]. The grain size for an individual alumina particle is between 0.5 μm and 1.5 μm with an average of 1.0 ± 0.3 μm, and the areal fraction of the alumina phase is estimated at 65 ± 1%. The areal fraction of the voids constitutes ~ 2% of the

image, and this correlates well with the results reported in a previous study by the authors [37]. This information is averaged over five locations for each surface investigated. As a result of the high content of ceramic phases and the relatively low ductility of intermetallic titanium aluminide phase, the cermet behaves in a brittle manner. Figure 1-b shows a FESEM image of a cleaned fracture surface of the as-received material. This surface was obtained from the as-received plate, where a piece was sectioned out to investigate the internal microstructure. Both equiaxed and columnar grain structures of the titanium aluminide phases are observed in the material, which correspond to the γ and α_2 titanium aluminide grains and (γ + α_2)-$TiAl/Ti_3Al$ lamellar structure (indicated by blue arrows), respectively. The red arrows in Figure 1-b point to the individual alumina grains which appear brighter than the gray titanium aluminide grains. All phases are identified through EDS analysis by comparing the relative elemental concentrations of aluminum, titanium and oxygen.

Figure 1-c demonstrates a representative bright field TEM image of the individual grains and the grain boundaries before experiments, showing clean and closely bonded alumina-alumina and titanium aluminide-alumina interfaces. This micrograph is obtained using a FEI Tecnai TF-20 FEG/TEM machine. The alumina grains and titanium aluminide grains are separated by dashed lines and marked on the micrograph. The empty spaces at the boundary of some alumina grains are the pores present in the material, and this confirms the observation of pore sites in the previous study by the authors [37]. In the micrograph in Figure 1-c, an alumina cluster is observed at the top right corner, which verifies the presence of alumina networks observed in the BSE-SEM image (see Fig. 1-a). Residual stress is also observed in alumina, as manifested in the darker contour lines connecting the boundaries of alumina grains (alumina composition confirmed with EDS). This is likely the result of rapid forming explosive SHS process used to fabricate the material, as well as

the mismatch in thermal expansion coefficient between alumina and titanium aluminide. In the alumina grain at the top left corner of Figure 1-c, dislocations (indicated by white arrows) are observed and they appear to bisect from the residual stress contour lines. This suggests some plastic deformation exists in the as-made material because of the highly energetic fabrication process. It is also observed that a microcrack (indicated by a red arrow) initiates from the tip of a dislocation and propagates through the alumina grain, but it is arrested by the titanium aluminide matrix. In the titanium aluminide phase, a duplex microstructure is observed, with some clean γ-grains (e.g., bottom left) and γ-grains with randomly orientated ($\gamma + \alpha_2$) lamellae (e.g., bottom right) (titanium aluminide phase compositions confirmed by EDS). Some dislocations are observed in between the lamellar structure, but most of the titanium aluminide grain surfaces are clean and free of plastic deformation.

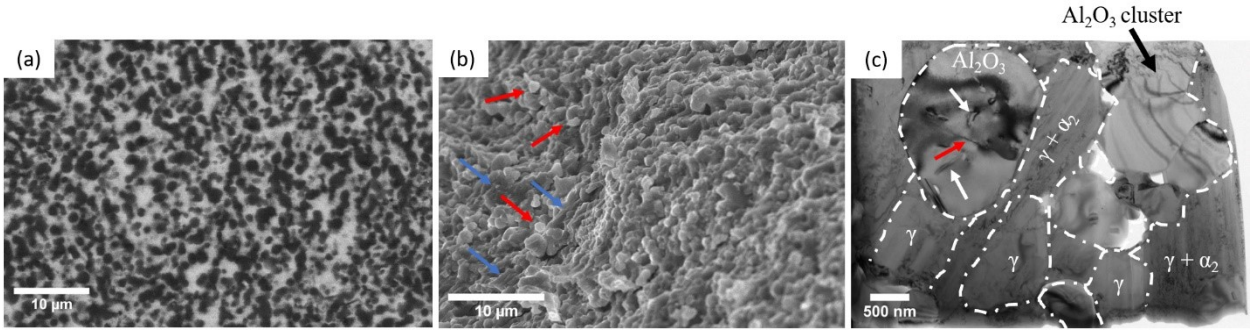

Figure 1: SEM and TEM micrographs examining the microstructural features of the as-received material. (a) BSE-SEM image on the polished surface showing the phase distribution and alumina clusters; the black regions correspond to the alumina phase and the white regions correspond to the titanium aluminide phases; (b) FESEM image on cleaned fracture surface showing shapes and sizes of alumina and titanium aluminide grains; the red arrows indicate the individual alumina grains, and the blue arrows point to the ($\gamma + \alpha_2$) – $TiAl/Ti_3Al$ lamellae. The titanium aluminide phase appears grayer in the image than the brighter alumina grains; (c) Bright field TEM image showing grain surfaces and grain boundaries. Residual stresses are present on most of the alumina grains, where dislocations (white arrows) and microcrack (red arrow) are observed on the alumina grain at the top left corner. Duplex microstructure of titanium aluminide phase, including clean γ grains and ($\gamma + \alpha_2$) lamellae on γ grains are obtained. No specific orientation of the lamellar structure is found in the as-received material.

2.2 Sample preparation for mechanical testing

Once materials were characterized, mechanical testing was performed. The material was provided as circular tiles (93 mm in diameter and 6.5 mm thick), from which cuboid specimens were machined via electrical discharge (EDM) for rate-dependent compression experiments. The cut specimens were post-polished down to a 0.1 microns surface finish to reduce effects by surface roughness and defects. Parallelism of the specimen surface (in terms of length along the loading direction) was carefully examined to be less than 1° on all surfaces. The uniaxial compression specimens (both quasi-static and dynamic) had dimensions of 2.3 mm x 2.7 mm x 3.5 mm. Loading was always carried out along the thicker (3.5 mm) side of the specimens, and this was in a direction that was parallel to the thickness direction of the as-received tile. The specimen dimensions were reduced by a factor of 1.5 following Farbaniec et al. [39], and they were chosen to compensate for both quasi-static and dynamic setups, as well as providing a sufficient surface area needed for good quality DIC analysis.

For postmortem analysis, fragments were recovered from the quasi-static and dynamic experiments, and they are used for microscopic diagnosis on both their surface and through investigation of internal damage. Parts of the fragments were investigated using SEM and TEM in their as-deformed state. Some fragments were cold mounted into epoxy resin and systematically polished for further study via SEM, TEM, and XRD. The mounted disks were polished down at least 500 μm from the surface to reveal the sub-surface damage, and the final surface finish was set at 0.1 μm finish.

3. Experimental setup

3.1 Microscopic diagnoses

3.1.1 Scanning electron microscopy

Scanning electron microscopy (SEM) analysis was carried out on both fractured and polished fracture surfaces to evaluate the microscale failure mechanisms under both quasi-static and dynamic loadings. The micrographs were taken using a Zeiss Sigma FESEM machine equipped with an energy-dispersive x-ray spectroscopy (EDS) setup. The machine was operated with the acceleration voltage set at 20 kV and a working distance of ~ 3.8 mm. An In-Lens detector was used to image the fracture features, including crack path, particle debonding, and plastic deformation mechanisms. The EDS probe was used to verify the compositions of the microstructural features presented in the corresponding field of view. No coating was needed for the specimen since conductivity was an inherent property of the intermetallic phase in the composite. The EDS data was analyzed using the AZtec software from Oxford Instruments. On average, at least two fragments per test were scanned to confirm the universality of the observed mechanisms, and micrographs revealing the representative fracture mechanisms were presented.

3.3.2 Transmission electron microscopy

High-resolution transmission electron microscopy (HR-TEM) was conducted on the material before and after testing to investigate the nanoscale deformation mechanisms, such as microstructural evolution, dislocation, and twinning. The TEM sample preparation and imaging were carried out at Eurofins EAG Laboratory located in California, USA [40]. The TEM samples were prepared from the same polished epoxy disks used for SEM analysis, and they were further prepared to be TEM-ready using the in-situ focus ion beam (FIB) lift out technique on a FEI Strata 400 Dual Beam FIB/SEM system. With in-situ SEM identification, an approximately 4.5 μm x 4.5

μm area of interest was extracted using FIB in the vicinity of a microcrack, where most deformation mechanisms are expected to be seen. Once the area of interest was defined, the samples were capped with sputtered Ir and e-Pt/I-Pt before sending for ion milling. Through ion milling, the final TEM lamella thickness was reduced to ~ 100 nm. After preparation, the samples were imaged with a FEI Tecnai TF-20 FEG/TEM operated at 200kV in bright-field (BF) TEM mode, high-resolution (HR) TEM mode, and high-angle annular dark-field (HAADF) STEM mode with a 0.2 nm nominal diameter STEM probe. Energy-dispersive x-ray spectroscopy (TEM-EDS) analysis was performed to identify the phase compositions, and the spectra were acquired in STEM mode using the FEI Osiris 4SDD system. Special care was taken to eliminate the artificial EDS peaks (i.e., C, Cu, and Ga), which could come from sample preparation. Selected area electron diffraction (SAED) patterns were analyzed at different locations within the titanium aluminide and alumina phases to investigate the symmetry of the crystallographic structures.

3.3.3 X-ray diffraction

Two-dimensional x-ray diffraction (2D-XRD) analysis was carried out to assess the crystallinity and identify the phases of the as-received material and fragments obtained after testing. The tests were carried out on a Bruker D8-Discover machine using Cu Kα beam source. The apparatus was operated at 50 kV and 1000μA. A Vantec 500 detector was used to produce two-dimensional frames, which were then processed using the Bruker Eva software to produce θ-2θ-equivalent spectra. A schematic of the test setup and the associated parameters is shown in Figure 2-a. This setup has been explained in more detail in the authors' previous publications [41, 42]. Figure 2-b shows a representative 2D frame. In any given frame, 2θ increases from right to the left, and Ψ values change along the denoted arcs. The distribution of intensity along Ψ signifies the randomness of the crystal orientations. In this representation, the solid arcs represent a completely

random angle distribution, and the dashed arcs represent preferred orientation arising from the crystalline texture or large crystallites (see Fig. 2-b).

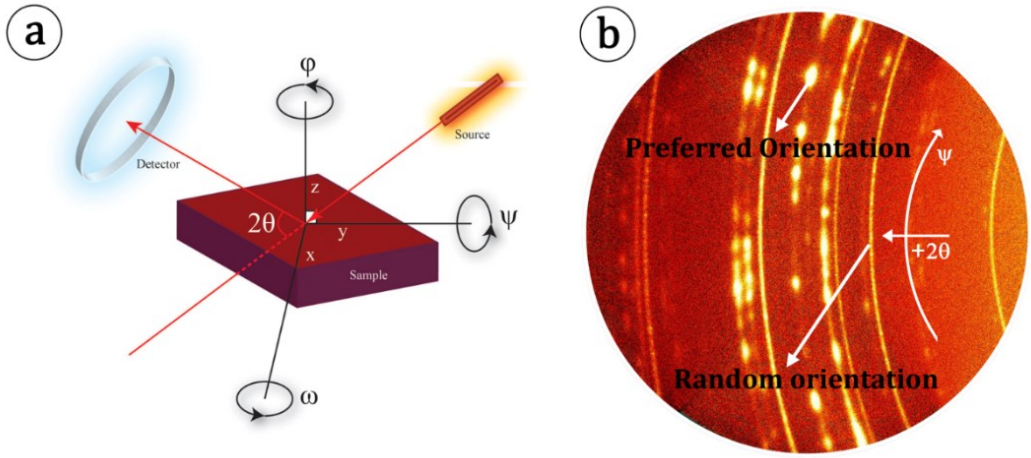

Figure 2: (a) Schematic of the 2D-XRD test setup and scan parameters; (b) A representative 2D frame showing typical arcs indicating a random orientation and a preferred orientation. The directions of integration (θ and Ψ) are from right to left and from bottom to top, respectively.

3.2 Mechanical testing

3.2.1 Quasi-static uniaxial compression testing

Quasi-static uniaxial compression tests were carried out on an MTS series 810 servo-hydraulic machine under displacement control with a nominal strain rate of 2 x 10^{-4} s^{-1}. Ti-6Al-4V titanium alloy jacketed tungsten carbide (WC) platens were used to reduce indentation from the specimen to the loading platens. Extreme pressure grease was applied between specimen and the WC platens to reduce the frictional effect and allow free lateral expansion. A 100 kN load cell and linear variable differential transformer were used to measure the force history and crosshead displacement, respectively. An AOS PROMON U750 high speed camera with a full resolution of 1280 x 1024 pixels was used to visualize the macroscopic surface deformation. High intensity LEDs coupled with optical light guides were used to obtain the high brightness and contrast in order to enhance the DIC strain field measurements. For data analysis, engineering stress and strain

were extracted from the MTS force data and DIC measurements, respectively. A matching of the peak stress and strain before failure was performed to obtain the stress-strain curves. In addition, both the frame rate of the camera and sampling rate of the MTS machine were set at 100 FPS and 100 Hz to minimize delay and matching errors. Detailed schematics and descriptions of the experimental setup can be found in the previous study by Li et al. [37]. In total, five representative curves for the quasi-static strain rate were acquired to demonstrate variability.

3.2.2 Dynamic uniaxial compression testing

The dynamic uniaxial compression tests were carried out on a modified version of a split Hopkinson pressure bar (SHPB). This technique was developed by Kolsky [43] initially for testing metals and modified later to compensate for brittle materials, such as ceramics and cermets [44 – 47]. One well-documented setup of the modified SHPB can be found in Hu et al. [48] on testing the dynamic failure of aluminum nitride. Detailed information on the setup used in the current study can be found in the previous study by Li et al. [38], and only the critical and updated components are mentioned here for completeness. In the current study, bars (including the striker, incident and transmitted bars) were made from Maraging steel C-350 with a common diameter of 12.7 mm. The specimens were placed between two impedance-matched Ti-6Al-4V titanium alloy jacketed tungsten carbide platens that were fixed to the opposite ends of the incident and transmitted bars, where the interfaces were lubricated with extreme pressure grease to reduce friction and allow the specimen to expand freely in the lateral dimension. A mild steel pulse shaper with a thickness of 0.0635mm was placed in front of the incident bar (against the striker) to create a ramped signal profile, while reducing the signal-to-noise level. This specific pulse shaper provided a proper rise time (8 to 10 μs) and ramp time for which the material could reach equilibrium under a single pass of the compressive loading wave, and the natural response of the

material can be captured. In this case, the total time of the event was within 20 μs. In addition, the air tank pressure was set to 50 psi in all tests, and the nominal strain rate was between 1 x 10^3 s^{-1} to 2 x 10^3 s^{-1}, depending on the response of material, variability in projectile speed, and uncertainty in strain measurements. For data acquisition, an HBM Gen3i High-Speed Recorder was used to capture the voltage signals at a sampling rate of 25 MHz. The transmitted signal was used to compute the stress-time profile.

An ultra-high-speed Shimadzu HPV-X2 camera was used to capture the failure process of the specimen during SHPB testing filming at 2 million frames per second with an exposure time of 200 ns, where 128 frames can be captured at the specified frame rate with a full resolution of 400 x 250 pixels. In this setup, a ring light from REL. Inc equipped with 32 high-power LED emitters with a focal point of approximately 13 inches was placed concentric to the camera lens to provide sufficient lighting to the specimen. This ring light would enhance the brightness and contrast, as well as providing an overexposure condition for the DIC analysis. Similar to quasi-static tests, DIC was used to obtain the global strain field in the dynamic tests. In this case, a K2 DistaMax lens from Infinity Photo-Optical Inc. was used to achieve a field of view, where the spatial resolution of the DIC analysis could be maximized. Stress and strain were matched in time by considering a common trigger point in the system. In total, five representative curves were acquired for comparison with the quasi-static tests, as well as demonstrating the variabilities in mechanical responses.

3.3 Digital image correlation technique and setup

Digital image correlation was performed to obtain the global strain field from the specimen surface in both quasi-static and dynamic tests. A brief summary on the theory behind DIC analysis is provided here because of the novelty of the technique to cermets and brittle materials in general.

In DIC analysis, an area of interest (AOI) is first defined, and displacements of the small subsets defined within the AOI are tracked as the specimen translates and deforms during loading [49]. The subsets in the deformed images are transformed to "match" the pattern in the reference image, and this "match" is performed as the total difference in gray scale intensity level at each interpolation point [49]. In each subset, a correlation peak is defined by interpolating the grayscale level at or between pixels, where the position of the peak provides a local displacement [50]. Therefore, the subset size is rather important in determining spatial resolution, and it is related to the specimen dimensions. However, there is no specific guidelines or published standards for determining the optimal subset size [51]. It is up to the user to decide an appropriate subset size which will output the necessary information as required. The selection of the subset size is discussed next.

In this study, VIC-2D 6 [52] software was used to map out the global strain fields in both quasi-static and dynamic tests. One advantage of the mentioned software is that the built-in algorithm provides a "suggested subset size" and noise level with the minimum estimated error based on the quality of speckle pattern and light intensity level using the reference frame. The software has been proven to be reliable by Sutton et al. [53] through calibration and error assessments. Considering the size of the specimen, applying a good speckle pattern on the specimen surface was one of the biggest challenges in the analysis process. A non-repetitive, isotropic, and highly contrasted speckle pattern is crucial in DIC analysis. Conventional speckle pattern kits, or other methods, such as regular spray paint, are not applicable on specimens with such small size. Coarse speckle pattern will force the subset size to be large enough to contain at least two distinct speckles while losing too much spatial resolution. From Giacomo and Luca [54], the minimum speckle size should exceed the image pixel size by a factor of 3 to 5, and speckles smaller than this will result in

aliasing. Shown in Figure 3-a and b are the typical speckle patterns obtained in the quasi-static and dynamic tests, respectively. Figure 3-a has a full resolution of 1280 x 1024 pixels (obtained with an AOS PROMON U750 high speed camera), and Figure 3-b has a full resolution of 400 x 250 pixels (obtained with a Shimadzu HPV-X2 ultra-high speed camera). The optimal speckle size has been chosen to be between 20 μm and 30 μm in both quasi-static and dynamic tests determined from their corresponding image pixel sizes. Isotropic and highly contrasted speckle patterns were able to be generated for both tests using a fine-point airbrush as is recommended in most DIC applications [53]. In this study, an ultra-fine point Harder and Steenbeck Infinity airbrush with a 0.15 mm diameter needle and nozzle was used to spray specialized metallic paint with particle sizes down to 0.1 micron onto the specimen surface. Output pressure from the compressor was set to 15 psi to ensure sufficient atomization of the paint. In addition, Jerabek et al. [55] indicated that a fine speckle pattern and light intensity gives a better result when it is under the condition of overexposure.

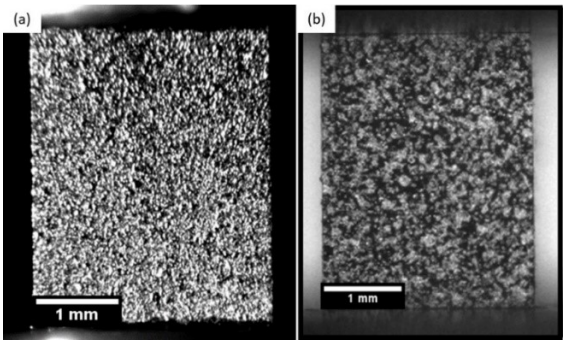

Figure 3: (a) A typical speckle pattern produced for DIC analysis for the quasi-static test. The compressive loading direction is vertical. (b) A typical speckle pattern produced for DIC analysis for the dynamic test. The compressive loading direction is vertical. Metallic paint was used for both cases in (a) and (b). The painted surfaces are always the biggest surface (2.7 mm x 3.5 mm) of the specimens. Isotropic and highly contrasted speckle patterns are obtained in both (a) and (b).

In the VIC 2D software, the "suggested subset size" for both quasi-static and dynamic tests were between 17 x 17 pixels and 25 x 25 pixels, which suggested a good quality of the speckle pattern. The "correlation step size" was manually tuned between 2 and 7 in each AOI to obtain smoother

strain profiles. During the analysis, the zero-normalized squared sum of squared difference (ZNSSD) method was chosen to perform the correlation as it was proven to be one of the more robust algorithms that would not be affected by the offset in light intensity and linear scale in the illumination lighting [50]. A Gaussian low pass filter was selected to eliminate the high-frequency signals and pre-smooth both reference (the first frame showing an undeformed state of the specimen) and deformed images (all the subsequent frames). This pre-smoothing will increase the accuracy of the measurement because it filters out the bias signals, according to Pan [56]. The "Optimized 8-tap" interpolation scheme in the software was selected which incorporated the highest order of the spline scheme. In post-processing, the average rigid body motion was removed to compensate for any vibration caused during testing and possible interferences with the cameras. Equations for the algorithm used and settings in the software are documented in Table 1 for readers' reference. The ZNSSD method (Eq. (1)) is an enhancement over the traditional sum of squared difference (SSD) first proposed as a correlation criteria by incorporating the mean intensity functions (Eq. (2) and (3)) and root sum of squared differences (Eq. (4) and (5)) regarding each reference and deformed frames. This will reduce the systematic errors, even if a linear transformation of the target subset gray intensity is made [49].

Table 1: Equations for the algorithm and software settings used for DIC analysis in both quasi-static and dynamic tests

Criterion: ZNSSD [49]	$C_{ZNSSD} = \sum_{i=-M}^{M}\sum_{j=-M}^{M}\left[\frac{f(x_i,y_j)-f_m}{\Delta f} - \frac{g(x_i',y_j')-g_m}{\Delta g}\right]^2$ (1) $f_m = \frac{1}{(2M+1)^2}\sum_{i=-M}^{M}\sum_{j=-M}^{M} f(x_i,y_j)$ (2) $g_m = \frac{1}{(2M+1)^2}\sum_{i=-M}^{M}\sum_{j=-M}^{M} g(x_i',y_j')$ (3) $\Delta f = \sqrt{\sum_{i=-M}^{M}\sum_{j=-M}^{M}\left[f(x_i,y_j)-f_m\right]^2}$ (4) $\Delta g = \sqrt{\sum_{i=-M}^{M}\sum_{j=-M}^{M}\left[g(x_i',y_j')-g_m\right]^2}$ (5)
Subset size	Between 17 x 17 pixels and 25 x 25 pixels
Step size	Between 2 and 7
Subset weights	Gaussian weights
Interpolation	Optimized 8-tap
Pre-filter	Low pass filter images
Consistency threshold (max margin) [pixels]	0.02
Confidence threshold (max margin) [pixels]	0.050
Matchability threshold (max margin) [pixels]	0.10

In Table 1:(x_i, y_i) and (x_i', y_i') are the coordinates of interpolation points in the reference (undeformed) and deformed frames, respectively; f and g refer to the intensity functions; $f(x_i, y_j)$ refers to the intensity function based on the displacement field in the reference frame; $g(x_i', y_i')$ refers to the intensity function in the deformed frames; and $(2M + 1)$ indicates the dimensions of the subset is are always odd.

4. Results

In this section, the results will be presented in the following order: 1. Stress-strain responses and macroscopic failure behavior; 2. Summary of compressive strengths at different strain rates; 3. Microscopy investigations on failure mechanisms; 4. Two-dimension x-ray diffraction exploring crystalline texturing. The results will be shown for both quasi-static and dynamic experiments.

4.1 Stress-strain responses and failure behavior

Shown in Figure 4 is the stress-strain responses obtained from five tests under quasi-static loading on the TiAl/Ti_3Al-Al_2O_3 cermet, named QS sp1 to QS sp5. The material is loaded uniaxially in the vertical direction in the inserts in Figure 4-b. Again, the stress is obtained from the MTS machine and the strain data is extracted by using DIC. The nominal strain rate in the quasi-static experiments is approximately 2 x 10^{-4} s^{-1} in all tests. This is estimated and confirmed by both taking the slope of the strain-time profile obtained from DIC analysis and tracking the edge displacements of the specimen among a sequence of images and then dividing by the corresponding time.

Shown in Figure 4-a are the quasi-static stress-strain behavior of the TiAl/Ti_3Al-Al_2O_3 cermet. Concaved stress-strain curves are observed for all tests with an initial linearly portion extended to approximately 0.002 strain. In this case, softening behavior on the instantaneous stiffness together with strain hardening of the TiAl/Ti_3Al-Al_2O_3 cermet is readily seen after a few microstrains. The stiffness of the cermet is measured at 0.001 strain by taking the slope of the stress-strain curves, which is measured between 230 GPa and 300 GPa, with an average of 267 ± 28 GPa. This method has been documented elsewhere in literature for measuring the stiffness of several types of cermets [15, 16]; the 0.001 strain point is chosen by fitting a second order polynomial to the stress-strain curve, where a near-constant region within 3% difference in slope is selected by taking the first derivative of the fitted polynomial. As a result, the 0.001 strain point is best suited for all five experiments, which also compensates the insensitivity in computing nanostrains at the beginning of the tests. The peak stress, which is often referred to as “quasi-static compressive strength,” for the quasi-static experiments is between 2700 MPa to 2900 MPa, with an average of 2780 ± 60

MPa. The failure strain, which is taken as the maximum strain value of the stress-strain curves, is between 0.013 to 0.018 for the quasi-static experiments, with an average of 0.0166 ± 0.0017.

Next, the post-peak failure and fracture behavior of the cermet is shown in Figure 4-b for quasi-static case in the form of high-speed camera images. Two still images are selected from two of the five tests for a representation of the representative shape and size of the structural fragments that remain after the experiments. The two data points shown on the x-axis of the stress-strain curves at higher strains indicate the strains where images are extracted (right after the peak load), and the colors are matching to the same color in the stress-strain curves. Large structural fragments are observed after failure, with column-like shapes and height (taken horizontally) between 1 mm and 2 mm in size. Lamellar tearing (indicated by red arrows) along the loading direction shown as bands can be seen on the fragmented surface. The axially-orientated splitting is believed to be one of the deformation mechanisms activated in the titanium aluminide matrix under compression. Small amounts of crack branching are observed along with these major cracks at the macroscopic scale, indicating that the failure is likely caused by a single or several dominant cracks. These fragments will be examined later in Figure 7 using SEM for identification of the fracture mechanisms and damage accumulation at the micro/nanoscale.

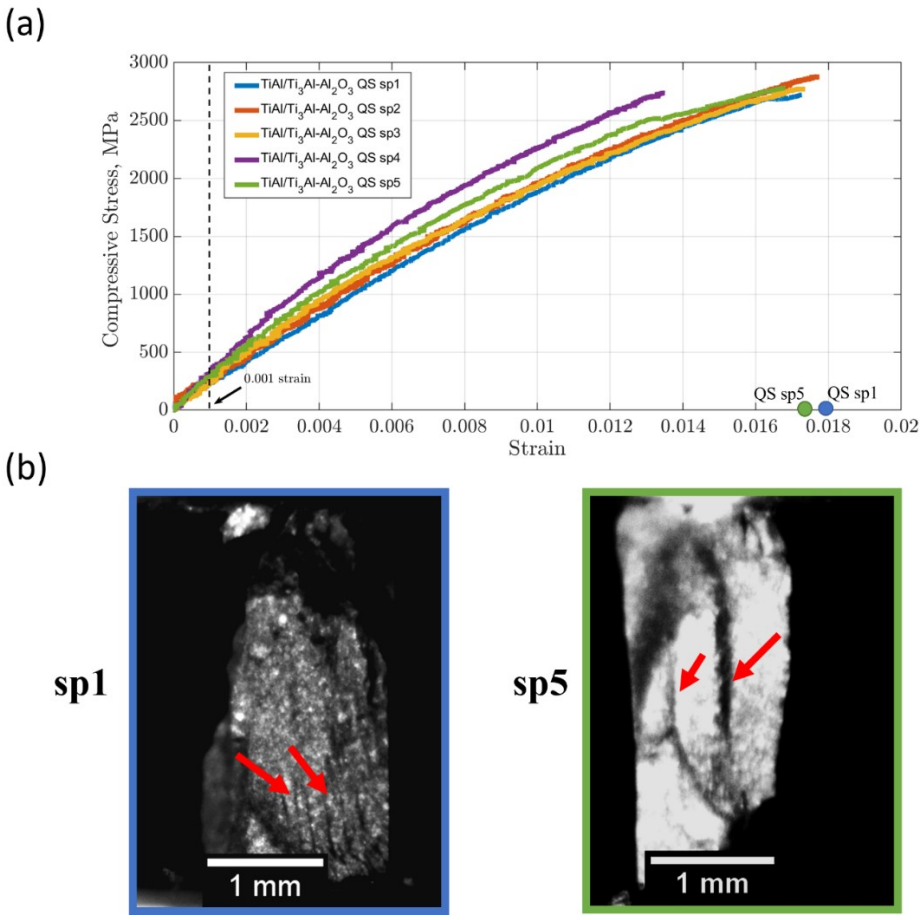

Figure 4: (a) Stress-strain curves of the TiAl/Ti_3Al-Al_2O_3 cermet under quasi-static uniaxial compression. The x = 0.001 strain line indicates where the stiffnesses are computed; (b) Still images showing typical post-peak structural fragments corresponding to two of the tests (QS sp1 & QS sp5) in (a). The data points on the x-axis in (a) are indications of when the images are extracted. The arrows shown in the fragment images are evidence of lamellar tearing along the loading direction, as one of the fracture modes under quasi-static loading.

Shown in Figure 5 is the material responses of the TiAl/Ti_3Al-Al_2O_3 cermet under high-rate loading, including stress-strain response (see Fig. 5-a) and ultra-high-speed camera still images showing fracture and fragmentation behavior (see Fig. 5-b). The material is uniaxially loaded in the vertical direction in the inserts in Figure 5-b. In total, five experimental results are plotted to demonstrate the representative stress-strain behavior, assess the variability in the material, and provide an adequate comparison with the quasi-static case. The strain rates in the dynamic experiments are between 1100 s^{-1} and 2000 s^{-1}. This is estimated by taking the average slope of

the upper bound and lower bound of the strain-time profile obtained through DIC analysis. From the figure, it is observed that the stress-strain curve increases linearly up to a certain yield point, where strain hardening starts to occur and a first peak is reached. After that, the second peak of the stress-strain curve is reached as a result of stress relaxation from the previous peak following by further strain hardening. The "alternating stress relaxation and strain hardening" behavior between two subsequent peaks is observed for the later peaks among all curves. The material is considered to be in unloading after the last peak in the stress-strain curve, and the post-peak stress-strain response is captured before fragmentation. In this case, a convex-shaped stress-strain behavior is observed, indicating that the material is continuously softening. Afterwards, the correlation is lost for even higher strains, and this is why the stress-strain curves do not return to zero stress in the figure. In all tests, at least two peaks are observed in each stress-strain curve, in which case a general trend of strength degradation in terms of peak stress values is observed with the first peak being the highest.

The highest peak, which is considered as the "dynamic compressive strength," is between 3000 MPa and 3500 MPa across the five curves, with an average of 3133 ± 265 MPa. It is observed that the compressive strength is approximately 1.3 times greater than their counterparts in quasi-static loading. The stiffness, taken at 0.001 strain given the same reason as the quasi-static case, is between 240 GPa and 270 GPa, with an average of 255 ± 11 GPa. The stiffness of the cermet remains in a good agreement in both loading conditions. The failure strain, extracted from the stress-strain curves right before the first primary crack appears, is between 0.020 to 0.030, with an average of 0.026 ± 0.0032. The failure strain is around 1.4 times the values obtained from the quasi-static case, with a seven order increase in strain rate from ~ 10^{-4} s^{-1} to ~ 10^{3} s^{-1}. It is observed that large variations in compressive strength and failure strain can be found in the material under

dynamic loading, corresponding to the high variability in mechanical response of the material. It is believed that the material microstructural variabilities and complexity of the fracture mechanisms under dynamic loading are responsible for the variability in the macroscale stress-strain responses, which is explored in subsequent sections.

Next, the in-situ failure and fracture behavior of the cermet under dynamic loading is examined by showing a series of ultra-high-speed camera images taken right before the onset of fragmentation (see Fig. 5-b). The loading is in the vertical direction. The corresponding experiment (DYN sp2) and strain (time) on the stress-strain curve is shown in Figure 5-a, where the dot represents the starting point of where the images are extracted. Images 1 and 2 constitute the last two frames of the stress-strain curve (see DYN sp2 in Fig. 5-a). The strain in the rest of the frames cannot be captured because of the loss in correlation in the DIC software. In image 1, the specimen is still mostly intact, where a horizontal crack is initiated at the middle of the specimen. In image 2, a splitting crack is also activated, and this propagates from the top edge of the specimen. It is deviated from the loading direction to the left at a ~ 45° angle towards the bottom left corner (indicated by red arrow). Simultaneously, a crack branch is formed at the center of the initial splitting crack and towards the bottom right corner (indicated by blue arrow). In image 3, the splitting crack and its corresponding crack branch have reached the bottom left and right corner of the specimen, respectively. Microcracks are activated at the top and bottom edges of the specimen at later times, and more crack branches are formed on the specimen surface. The specimen is at the onset of fragmentation at ~ 18 μs (outside the DIC capture zoom). In image 4, the specimen starts to shatter, and more crack branches are observed on the surface. The cracks begin to interact and coalesce to form bigger crack networks at ~ 20 μs.

Image 5 shows the fragmentation behavior of the TiAl/Ti_3Al-Al_2O_3 cermet under dynamic loading. Much smaller structural fragments are observed in the dynamic experiments than in the quasi-static case, where the specimen fractured into irregular pieces after coalescence of the cracks. The crack speed in the dynamic experiments are between 2200 m/s to 3100 m/s, with an average of 2550 ± 480 m/s. This is estimated by considering the first two or three cracks in all of the videos. The speed is measured by tracking the position of the crack tip and length of the crack and taking the average over a few subsequent frames. Note that the crack speed in the MTS tests is inaccessible for the current setup; therefore it is omitted in this study.

Lastly, we show a sequence of representative still images taken from a dynamic experiment using the unpainted specimen (see Fig. 5-c) to illustrate a texturing phenomenon that is not as evidently seen with the painted surface. Image 1 is taken at the very beginning of the test where the specimen is still intact. In image 2, surface texturing (circled) starts to occur with higher concentrations at the middle region of the specimen, with no specific orientation determined. This image is taken near the first peak in stress of its corresponding curve (~ 0.01 strain). In images 3 and 4, the size of the textures continues to grow, where splitting crack and crack branches are observed on the surface. Image 4 shows the onset of the fragmentation, where a crack network is formed from crack growth and coalescence. These images are taken around the same timeframe (or ~ 0.03 strain) as image 3 in (b), where the splitting crack has propagated through the whole specimen, and the fragmentation has begun. It is believed that the surface texturing phenomenon observed under dynamic loading (not in quasi-static loading) is responsible for or the consequence of some observed rate-dependency and hardening/softening behavior in the stress-strain curve. We further investigate the associated dynamic failure mechanisms using XRD, SEM, and TEM in a later section.

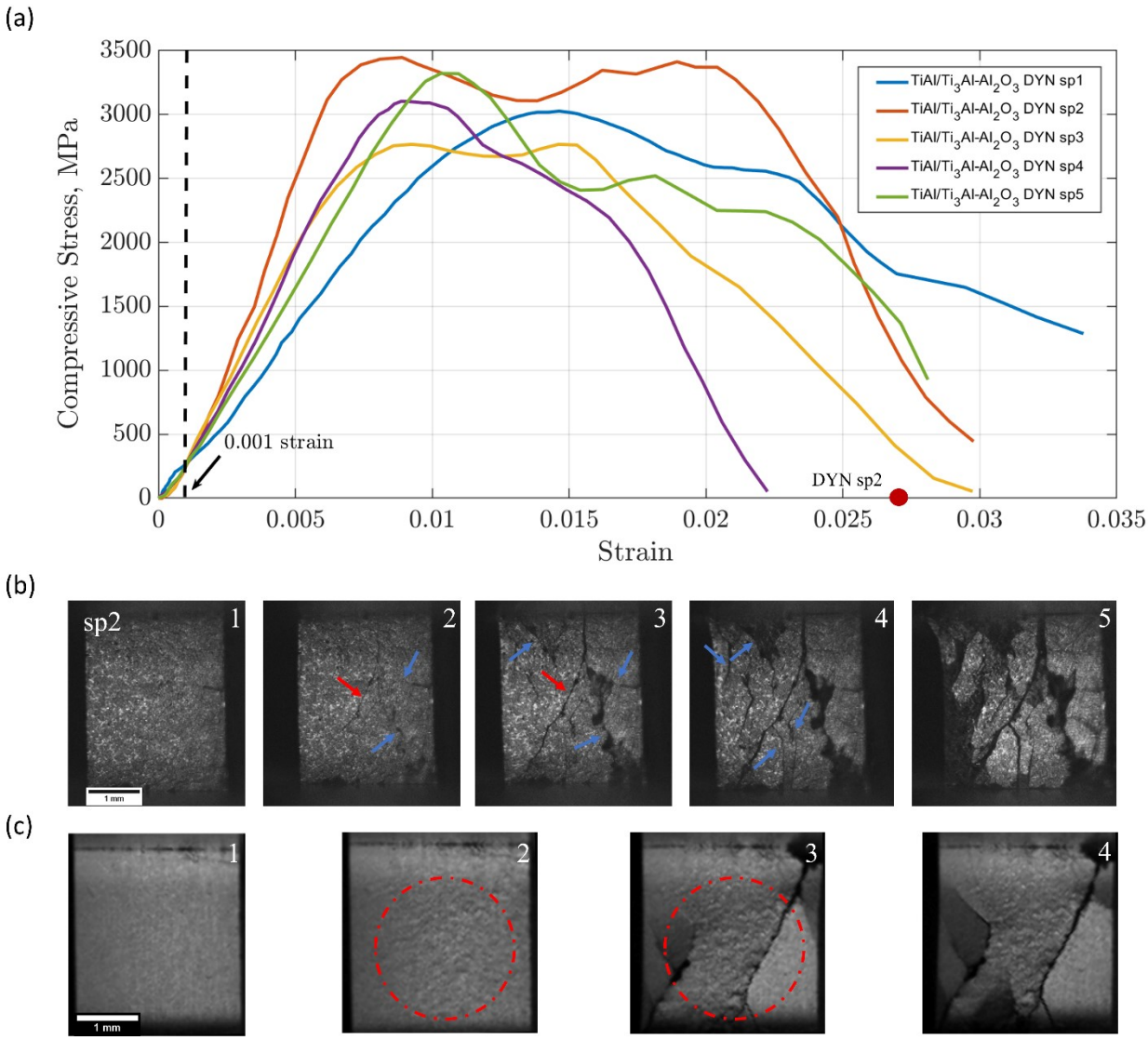

Figure 5: (a) Stress-strain curves for dynamic uniaxial compression tests. The x = 0.1% strain line indicates where the stiffnesses are computed for each curve; (b) A sequence of still images of sample DYN sp2 showing typical post-peak fracture paths of the cermet under dynamic loading. The red dot shown on the x-axis in (a) indicates the starting point of when the images are extracted. The red arrows in the images in (b) show a primary split crack along the loading direction, and the blue arrows show crack branching from the primary cracks, as well as cracks activated during further loading; (c) A sequence of representative still images taken from the tests using unpainted specimen to reveal the surface deformation features. The red circle highlights where the texturing is observed on the specimen surface. Splitting and branching cracks are also identified that are similar to (b).

4.2 Summary of the compressive strength at different strain rates

Shown in Figure 6 is the summary of the compressive strength (taken as the peak stresses) plotted against strain rate for the $TiAl/Ti_3Al\text{-}Al_2O_3$ cermet. As mentioned, the quasi-static compressive

strength has an average of 2780 ± 60 MPa at an average strain rate of 2 x 10^{-4} s^{-1}. In all eight dynamic experiments (including the five experiments plotted in Figure 5 and three unplotted), the compressive strength is between 3000 MPa and 3800 MPa with an average of 3410 ± 247 MPa, with strain rates between 1 x 10^{3} s^{-1} and 2 x 10^{3} s^{-1}. On average, the compressive strength increases approximately 1.3 times as the strain rates increases from ~ 10^{-4} s^{-1} to ~ 10^{3} s^{-1}. Notable is the increase in variability of the strengths for the higher strain rate, and the apparent high rate sensitivity at the higher strain rates.

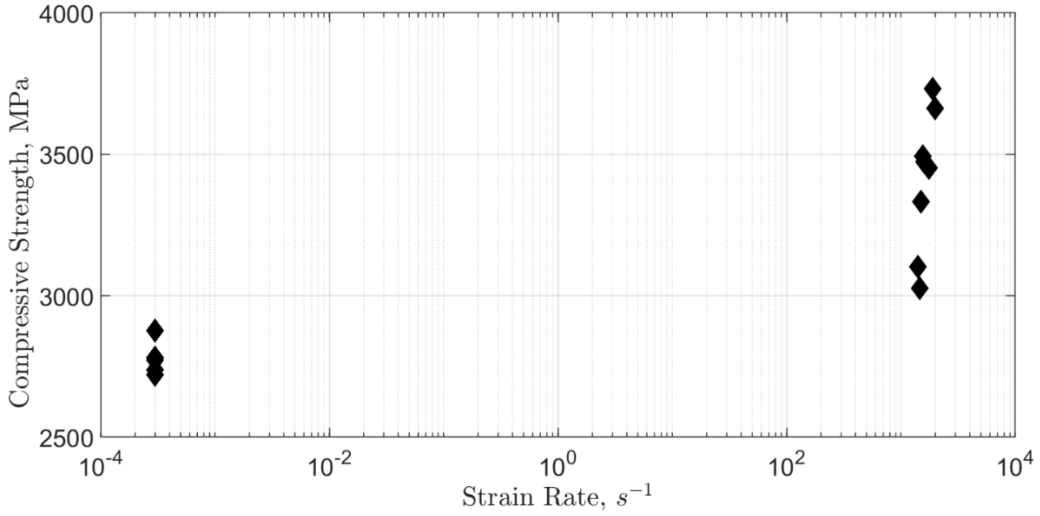

Figure 6: Semi-log plot of the uniaxial compressive strength of the TiAl/Ti_3Al-Al_2O_3 cermet as a function of the strain rate. The dynamic compressive strength is approximately 1.3 times the quasi-static compressive strength with an seven order increase in strain rate (from ~ 10^{-4} s^{-1} to ~ 10^{3} s^{-1}). In addition, the material appears to be more rate sensitive at high strain rates.

4.3 Microscopic diagnosis

4.3.1 Micro/nanoscale failure mechanisms under quasi-static uniaxial compression

Fractography studies have been carried out on the fragments retrieved from both loading conditions using SEM and TEM to determine the rate-dependent failure mechanisms of the TiAl/Ti_3Al-Al_2O_3 cermet. Shown in Figure 7a – c is a set of representative micrographs taken of the fractured surfaces recovered from the quasi-static tests. Shown in Figure 7-a is the global

435 FESEM image of a fracture surface showing a microcrack developed in the vicinity of the primary axial crack, where the yellow arrows indicate the direction of compressive loading. It is observed that the crack propagates through the darker phase (titanium aluminide) and passes along the boundary of the brighter particles (alumina, indicated by blue arrows). This is referred to as intergranular fracture in some of the literature on the fracture mechanisms of cermets (e.g., Kaplan
440 et al. [57]), where cracking happens in the binding matrix (titanium aluminide in this study). Small amounts of cleavages are observed near the cracks on the darker phase (indicated by blue arrows), which is an additional proof of brittle fracture in the material. It is observed that there is a minimal amount of transgranular fracture (cracking through the alumina particles) under quasi-static compressive loading, and this has been validated by investigating eight locations in five typical
445 fragments recovered from the quasi-static tests. Figure 7-b shows a magnified view of a fracture surface which demonstrates interfacial fracture, particle debonding, and dimpling being activated during quasi-static loading (indicated by white arrows). The red arrows indicate some typical post-deforming features that are created by these mechanisms. It is observed that grain boundary delamination and particle pull-out are two major phenomena appearing on the quasi-static fracture
450 surface, and these have been seen at a significant scale on all fragments. Distinct cleavage facets (indicated by a white arrow in Fig. 7-b) are observed inside the holes where the particles are being pulled out. These cleavage facets are believed to be formed mainly via interfacial debonding. These cleavages can be differentiated from the lamellar-shaped pattern appearing in the matrix by the wave pattern that is formed inside the craters. Ductile dimples are also observed inside the darker
455 phase, but not in a significant amount. Additionally, the grain boundaries between particles seem to remain intact, and minimal delamination at the particle boundaries are observed throughout all the fragments. Figure 7-c demonstrates a triple junction region (indicated by a red arrow) formed

by branched cracks, and similar mechanisms such as grain boundary delamination and particle pull-out are observed in the vicinity of the cracks. It is also observed that the cracks propagate by tracing the particle boundaries along the crack path, where no particle-particle interfaces are interrupted by the cracking.

Due to the uneven nature of the fracture surface in Figure 7-c, contrast is not enough to identify cracking from either the alumina phase or the equiaxed gamma titanium aluminide phase. In order to verify the observation of intergranular cracking, EDS is applied to identify the relevant phases from elemental mapping. Figures 7-d to f show the corresponding elemental maps of Figure 7-c, where the major elements Al, O, and Ti are mapped to investigate the phases along the cracks and at the triple junctions. The brighter intensities correspond to higher relative concentrations. Shown in Figure 7-d is the EDS map of aluminum. This element appears in all TiAl, Ti_3Al, and Al_2O_3 in the cermet being investigated, with higher concentration in the alumina phase. A clear crack path in the Al map corresponding to the SEM image can be identified in Figure 7-d (indicated by a yellow arrow), with higher concentrations reflected on the particles along the path, which indicates a high possibility of an alumina phase. The region at the triple junction (indicated by a blue arrow) exhibits a lower amount of Al, which may correlate to either the TiAl or Ti_3Al phase. This can be further clarified with the O map shown in Figure 7-e. It is observed that the particles that have a higher concentration of Al correspond to regions with a higher concentration of O, and these are likely the ($\gamma + \alpha_2$) titanium aluminide lamellae. The regions at the triple junction contain no detectable oxygen, and these are likely the γ-TiAl phase. The Ti map shown in Figure 7-f does not reveal the crack path clearly because of the high electron absorption rate of titanium. By superimposing the crack position with the map, the regions with high concentrations of Al and O correspond to regions with no concentration of Ti, and the regions at the triple junction contain a

high concentration of the Ti element. In addition, a trace amount of oxygen is detected at the regions where titanium exists, and this is the ($\gamma + \alpha_2$) lamellar structure due to the higher oxygen precipitation at the interfaces [33]. Combining these observations, we conclude that the intergranular fracture happens within the titanium aluminide phase (possibly in both γ-TiAl and
485 α_2-Ti_3Al), and the region at the triple junction is covered with equiaxed γ-TiAl grains.

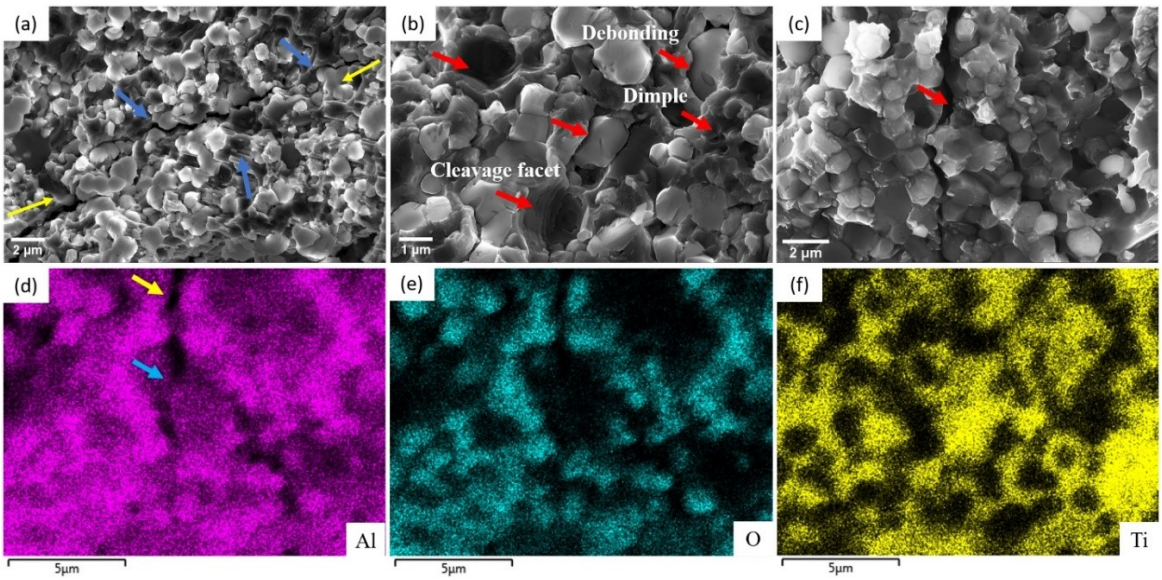

Figure 7: Micrographs taken on the fracture surface showing the fractography of the TiAl/Ti_3Al-Al_2O_3 cermet under quasi-static uniaxial compression. (a) A global view of the crack propagation, where the yellow arrows indicate the compressive loading direction, and the blue arrows indicate the intergranular fracture in the titanium aluminide matrix and cleavage in the titanium aluminide lamellar planes; (b) A magnified view in the vicinity of the crack in (a) showing typical deformation mechanisms, including grain boundary delamination, particle pull-out, and dimpling; (c – f) FESEM image with the corresponding EDS maps showing the phases where the intergranular fracture happens. (c) FESEM micrograph showing an intergranular crack passing through the field of view, where a triple junction is formed; (d) Distribution of the Al element in the FESEM image; (e) Distribution of the O element in the FESEM image; (f) Distribution of the Ti element in the FESEM image. In each EDS map, a brighter color indicates a higher concentration of such element.

4.3.2 Micro/nanoscale failure mechanisms under dynamic uniaxial compression

In this section, fractography studies are conducted on the TiAl/Ti_3Al-Al_2O_3 cermet fragments recovered from the dynamic experiments. Both fracture surfaces and polished fracture surfaces are investigated to determine failure mechanisms and compare with the quasi-static test results. Shown in Figure 8a – b is a set of FESEM micrographs taken of polished fracture surfaces that are used

to probe the sub-surface damage mechanisms. In Figure 8-a, a microcrack propagates through the field of view from the top to the bottom of the image (pointed out by a white arrow), with the darker phase being alumina. It is observed that the crack passes both along and through the alumina phase, where a combination of intergranular and transgranular cracking are observed to occur simultaneously under dynamic loading. Voids are also observed in the crack path, and it appears as though there are some void growth and coalescence ahead of the crack tip. In addition, extensive particle fracture and particle-particle interface fracture are observed around the microcrack (indicated by red arrows). Some of the fractures occurring within a cluster of alumina particles remain in the particles and do not propagate further into the matrix. Different from what is observed in the quasi-static case, it is believed that transgranular cracking is one of the dominant failure mechanisms under dynamic loading. Figure 8-b investigates the density of the void growth (shown as dark color) under dynamic loading by using a larger scale field of view. The areal fraction of the voids constitutes ~ 4% of the image, for which void growth is observed across all polished fragment surfaces being investigated with a heterogeneous distribution. The areal fraction of voids is approximately twice as much as that are computed in the as-received material (see Fig. 1-a). It is also noted that the voids tend to grow within or surrounding the alumina phase. This extensive void growth and particle cracking are not observed on the polished fracture surface under quasi-static loading, and so is believed to be unique for the dynamic experiments.

Figure 8-c and d show FESEM micrographs taken on the facture surfaces of the dynamic fragments. Shown in Figure 8-c is a typical fracture plane observed under dynamic compressive loading. Extensive cleavages are identified in the titanium aluminide phase compared to the quasi-static case (see Fig. 7-a), which is believed to correspond to the lamellar tearing in the ($\gamma + \alpha_2$) lamellar plane. In addition, a significant amount of ductile dimpling is observed on the fracture plane. In

Figure 8-d, a magnified view is used to probe different fracture mechanisms activated under dynamic loading. It is observed that three types of the fracture mechanisms can exist concurrently in a single microcrack: 1. intergranular fracture; 2. matrix fracture; and 3. particle fracture. This supports the extensive particle fractures and inter/transgranular cracking observed in Figure 8-a on the polished fragment surface.

Shown in Figure 8-e is an image of a microcrack that propagates through the field of view from left to right with the corresponding aluminum elemental map (Fig. 8-f). Pointed out by the red arrow is a site where high concentrations of Al are present on the upper side of the crack, while lower concentrations of Al are present on the lower side of the crack. It is suggested that intergranular cracking occurs along an alumina particle (upper side) and through the titanium aluminide matrix (lower side). No evidence of transgranular cracking can be found on fracture planes like this, and this is expected because typically lower energy is needed for a particle to delaminate from the matrix rather than for it to fracture. In addition, a hole formed from particle pull-out (see Fig. 8-e) is identified within the fractured titanium aluminide plane to supplement the observation.

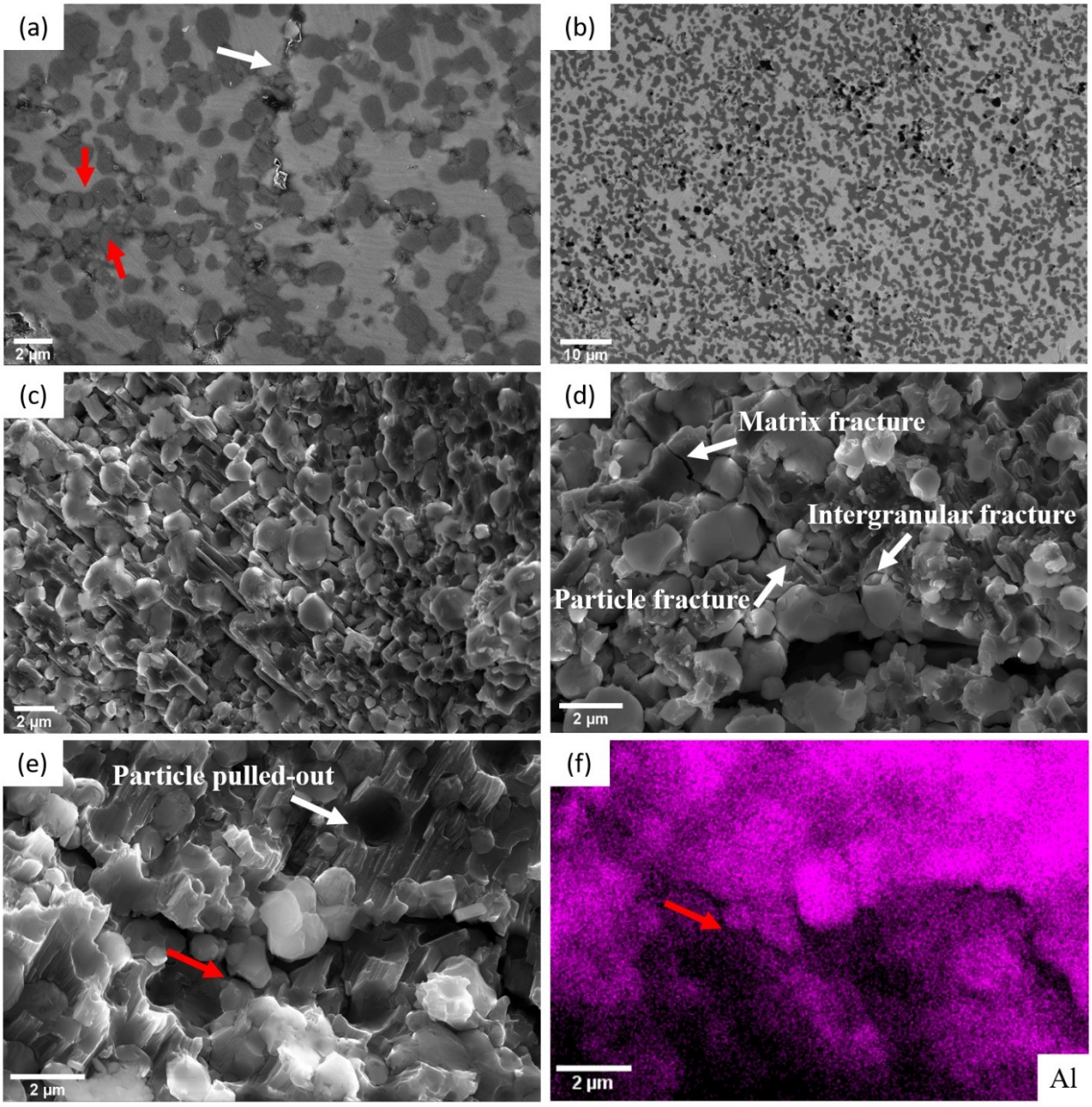

Figure 8: Micrographs showing the fractography of the TiAl/Ti_3Al-Al_2O_3 cermet under dynamic uniaxial compression. (a – b) FESEM images taken on the polished fracture surface revealing the sub-surface damage of the cermet. (a) Extensive particle fracture and particle interface fracture are observed in the alumina phase (phase with darker color), and a crack (indicated by a white arrow) propagates along and through the alumina particles with void growth identified on the crack path; (b) A global view of the sub-surface damage on the polished fracture surface showing the density of the void growth (shown as dark color) under dynamic compressive loading. (c – e) FESEM images taken on the fracture surface showing different deformation mechanisms activated in the material. (c) A typical fracture plane under dynamic loading showing extensive amounts of cleavage in the titanium aluminide matrix; (d) A magnified view on three of the major fracture sites in the material, including particle fracture, matrix fracture, and intergranular fracture; (e) A microcrack propagates through the field of view horizontally with (f) the corresponding Al element map to identify the phases along the crack. Particle pull-out is also observed on the fracture surface in (e).

Next, the microstructural evolution of the TiAl/Ti_3Al-Al_2O_3 cermet under dynamic uniaxial compressive loads are probed by using TEM coupled with SAED and EDS. Shown in Figure 9-a is a bright field TEM micrograph showing a global view of the postmortem microstructure. The brighter regions in the micrograph are the alumina clusters, and the darker regions surrounding the clusters are the titanium aluminide phases. The empty spaces represent the pores already existing in the as-received material or voids induced by grain boundary delamination from loading (note the void growth observed in Fig. 8-b). It is observed that the titanium aluminide phase exhibits a globally lamellar structure, with an orientation approximately 30° with respect to the horizontal plane (indicated by the red arrow). The difference in grayscale color between the lamellar structures suggests the activation of different deformation mechanisms, which will be discussed in Figure 10. Figure 9-b shows the corresponding SAED pattern taken at the circled location in Figure 9-a, and the crystalline planes are indexed from the diffracting patterns taken at that location. Two phases are identified from the SAED analysis, termed the γ-TiAl and α_2-Ti_3Al phases, and they appear as alternating γ and α_2 titanium aluminide lamellae (denoted as γ/α_2 lamellae). This alternating pattern is confirmed by the lines (orientation specified) formed from the diffracting "dots" with alternating sizes in Figure 9-b.

Figure 9-c to Figure 9-e confirm the observation in Figure 9-b by providing a magnified view of the γ/α_2 lamellae with corresponding EDS maps showing the compositions of the individual lamella. Figure 9-c is a bright field TEM micrograph focused at the alumina-titanium aluminide phase boundary, where the phase boundary is outlined by dashed lines in the figure. The alumina phase appears as black on the right hand side, whereas the γ/α_2 lamellar structure appears as white or gray on the left. It is observed from the Al elemental map (see Fig. 9-d) that higher concentrations of Al element correspond to the gray lamellae in Figure 9-c, and lower

concentrations of Al element correspond to the white lamellae in Figure 9-c. In addition, higher concentrations of the Ti element in Figure 9-e corresponds to the white lamellae in Figure 9-c, and lower concentrations of Ti in Figure 9-e corresponds to the gray lamellae in Figure 9-c. Taken together, all of the evidence suggests that the white lamellae in Figure 9-c are the α_2-Ti_3Al phase, where higher relative concentration of Ti and lower relative concentration of Al are shown. Consequently, the gray lamellae in Figure 9-c are the γ-TiAl phase, where lower relative concentration of Ti and higher relative centration of Al are revealed. Large variations of the lamella width are observed. The γ lamella width is between 10 nm to 80 nm with an average of 35 ± 19 nm, and the α_2 lamella width are between 5 nm to 60 nm with an average of 31 ± 21 nm. Lamella width is defined by drawing a line perpendicular to the lamella boundaries (indicated by the double arrow in Fig. 9-c), and these measurements are averaged over at least 15 locations for each phase. Shown in Figure 9-f is a high-resolution TEM image demonstrating the lattice structure of an adjacent pair of γ/α_2 lamellae. The lamellar boundary is indicated by the dashed red lines. The γ lattice exhibits a structure similar to an elongated rectangle, whereas the α_2 lattice shows a structure surface similar to a square. This is justified from studying the crystalline structure of the γ-TiAl and α_2-Ti_3Al, for which they have an ordered face-centered tetragonal $L1_0$ structure and an ordered hexagonal DO_{19} structure, respectively [58]. Thus, it is concluded that the microstructure of the titanium aluminide phase of the current cermet has evolved from a duplex structure (see Fig. 1-c) to a fully lamellar structure with alternating γ/α_2 lamellae under dynamic compressive loading.

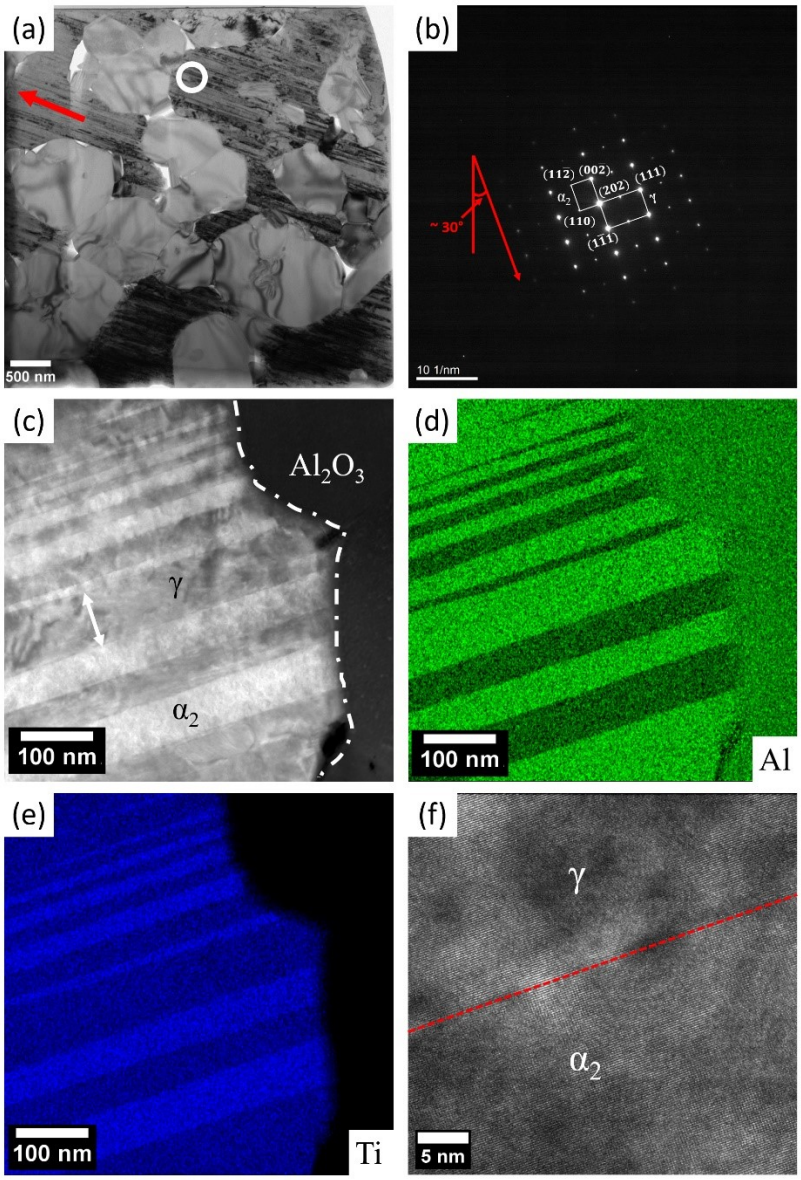

Figure 9: TEM micrographs showing microstructure evolution under dynamic uniaxial compressive loads. (a) A global view of the TEM lamella showing the alumina clusters (lighter regions) and the titanium aluminide lamellae (darker regions). The orientation of the titanium aluminide lamellae (red arrow) is approximately 30° with respect to the horizontal plane. (b) SAED pattern corresponding to the circled region in (a) identifying the presence of γ and α_2 lamellae. The orientation is specified in the figure, and it corresponds to the lamellar orientation in (a). (c – e) Bright field TEM on the alumina-titanium aluminide boundary and the corresponding EDS maps showing the lamellae compositions. The alumina-titanium aluminide boundary is identified by dashed lines in (c). In each EDS map, a brighter color indicates a higher concentration of the corresponding element. (f) High-resolution TEM showing crystalline lattice structure of an adjacent γ/α_2 lamellae. The grain boundary is indicated by a dashed red line.

Finally, the nanoscale deformation mechanisms of the $TiAl/Ti_3Al$-Al_2O_3 cermet under dynamic uniaxial compressive loads are investigated. Shown in Figure 10 are the bright field and high-resolution TEM micrographs that demonstrate different deformation mechanisms activated in the alumina phase, at the alumina-titanium aluminide phase boundary, and between the γ/α_2 lamellae. In Figure 10-a, residual stress is observed across all alumina clusters, and they are manifested as the dark contour lines connecting the grain boundaries. This residual stress could be the consequence of manufacturing process (also seen in the as-received material in Fig. 1-c) or high pressure loading. Dislocations (indicated by white arrows) are observed on the alumina grains, and they appear to be initiated either from the grain boundary or from the residual stress contour lines. It is observed that these dislocations are often localized features, where they do not pileup and distribute evenly across the alumina clusters. A microcrack (indicated by a red arrow) is observed to initiate at the tip of a dislocation and propagate through the alumina grain, and it is arrested at the alumina-titanium aluminide boundary. No twinning is observed on any part of the investigated alumina phase, and most of the grains are free of plastic deformation. In Figure 10-b, nano-twins (indicated by yellow arrows) are observed at the lamellar boundaries in the titanium aluminide phase. The twinning is identified by the periodic pattern of the structure as well as their orientation reference to the γ/α_2 lamellae. The twin boundary structures and their corresponding planes are omitted here because of the difficulties in determining the orientation of the fragments with respect to the deformation axis, which are recovered after an explosive failure under dynamic loading. These nano-twins appear to be connected at the lamellar boundaries and formed curved surfaces that extend into the adjacent lamellae. In addition, alumina-titanium aluminide grain boundary delamination is observed, where a microcrack is formed and propagates along the boundary.

Shown in Figure 10-c is a bright field TEM image focused on the dislocations in between the γ/α_2 lamellae. Three dislocation phenomena are observed and indicated in the figure: 1. Dislocation tangling, which usually occurs in the middle of the lamella (in this case in the γ phase), appears as a dark cloud of randomly-orientated dislocations [59]; 2. Dislocation network that also occurs in between the lamella. The dislocations are crossing and interconnected with each other to form a meshed structure [60]; 3. Dislocation wall that appears as black dots accumulated together and occurs at the boundary of the lamella [59]. Unlike the localized dislocation regions in the alumina grains, these dislocation features are shown as global plastic deformation in the titanium aluminide phase (see Fig. 9-a). In addition, twin boundaries (indicated by yellow dashed lines) are pointed out in one of the γ lamella. Lastly, shown in Figure 10-d is a high-resolution TEM micrograph looking at the alumina-titanium aluminide boundary. Phases are identified in the figure. Dislocation pileups are observed at the location, which have characteristics similar to the dislocation wall. After careful examinations, it is concluded that most of the nanoscale plastic deformation mechanisms take place in the titanium aluminide phase under uniaxial compression for strain rates between 1000 s^{-1} and 2000 s^{-1}.

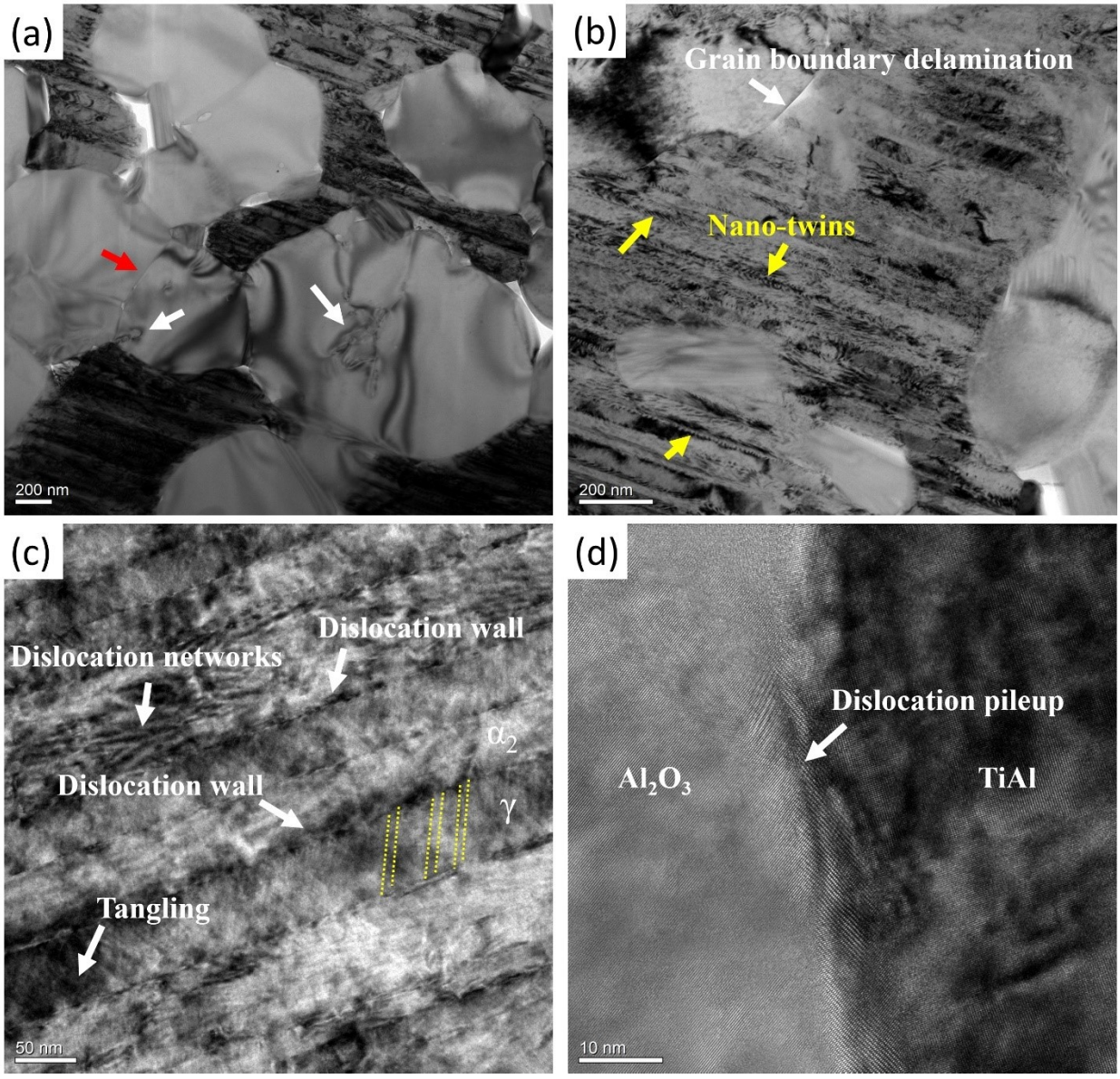

Figure 10: Bright field TEM micrograph showing the deformation mechanisms activated under dynamic uniaxial compressive loads. (a) Residual stress (appeared as dark contour lines) and dislocations (indicated by white arrows) are observed on the alumina grains. A microcrack (indicated by a red arrow) is initiated from the dislocation tip and propagate through the alumina grain. (b) Delamination occurs at the alumina-titanium aluminide grain boundary. Nano-twins (indicated by yellow arrows) are observed crossing the titanium aluminide lamellar boundaries and forming periodic curved structures. (c) Different types of dislocation activities, including dislocation walls, networks, and tangling are observed within titanium aluminide lamellae and at the lamellar boundaries. (d) High-resolution TEM micrograph showing dislocation pileup at the alumina-titanium aluminide grain boundary.

4.4 X-ray diffraction

Two-dimensional x-ray diffraction is applied as a way to examine possible phase changes and crystalline texturing evolution in the TiAl/Ti_3Al-Al_2O_3 cermet before and after experimentation. Shown in Figure 11-a is the $\theta - 2\theta$ equivalent spectrum plot for the as-received material, and of fragments taken after quasi-static and dynamic experiments. In this case, the spectrum plot of the as-received material is used as a reference to compare with the spectrums of both post-deformation frames from the quasi-static and dynamic tests. The major peaks corresponding to the three phases (i.e., γ-TiAl, α_2-Ti_3Al, and Al_2O_3) are identified on the spectrum, and the corresponding plane related to each peak is labeled adjacent to the peak. On the spectrum of the quasi-static fragment, no additional peak is observed, and no phase change occurs under quasi-static loading. An amorphous peak is observed between 10° and 20° in the spectrum of the dynamic fragment, and it is superimposed with the first α_2-Ti_3Al peak in the pristine material at around 17°. No such phenomenon is observed under quasi-static loading, and no additional phase changes occur (in terms of additional or vanishing peaks) in the material under dynamic loading. Note that amorphization occurs in other materials under specific conditions, usually under decompression from an extremely high pressure (e.g., B4C under shock wave loading [61]). In this case, even though amorphization did occur in the TiAl alloys under high pressure torsion [62], we do not believe the stress level in our experiments is sufficient for a pressure-induced type of amorphization to occur. The specific reason for the amorphous behavior needs to be further examined in future studies. Lastly, the absence of phase change is confirmed by checking the phase ratio of each phase (i.e., γ-TiAl, α_2-Ti_3Al, and Al_2O_3), for which all peak intensities corresponding to each phase are normalized by the highest peak of that phase. In total, two sets of samples are scanned to ensure the repeatability of the results.

Next, shown in Figure 11-b is the two-dimensional diffraction frames revealing the crystalline texturing evolution of the: as-received materials (top), and of a polished fracture surface taken from a quasi-static test (middle), and a dynamic test (bottom). In the frame of the as-received material (top frame), all arcs are mostly solid, which indicates all γ-TiAl, α_2-Ti_3Al, and Al_2O_3 phases are in a randomly-orientated polycrystalline form (no preferred crystallographic orientation). The brightest contour line, which corresponds to the highest peak in Figure 11-a, is a superimposed peak consisting of both γ-TiAl and α_2-Ti_3Al. It is observed that this superimposed titanium aluminide phase is in its randomly orientated state in the as-received material. In the frame of the quasi-static fragment, some degrees of crystalline texturing occur, and this is manifested as changes from solid arcs to mildly dashed arcs in the middle figure. In the quasi-static fragment, it is observed that all arcs corresponding to both γ-TiAl and α_2-Ti_3Al phases transform from their random polycrystalline structure to a crystalline textured structure (as indicated by the dashed arcs), whereas the alumina phase remains in its randomly orientated form (as indicated by the solid arcs). Similarly, the crystalline texturing of the titanium aluminide phase keeps evolving and becomes more textured (and less random) in the dynamic fragment (see Fig. 11-c). Less preferred crystallographic planes are observed, and this is shown as the decreasing number of the dashed arcs in the 2D frame. For the dynamic experiment, the alumina phase remains in its randomly orientated polycrystalline structure under dynamic loading.

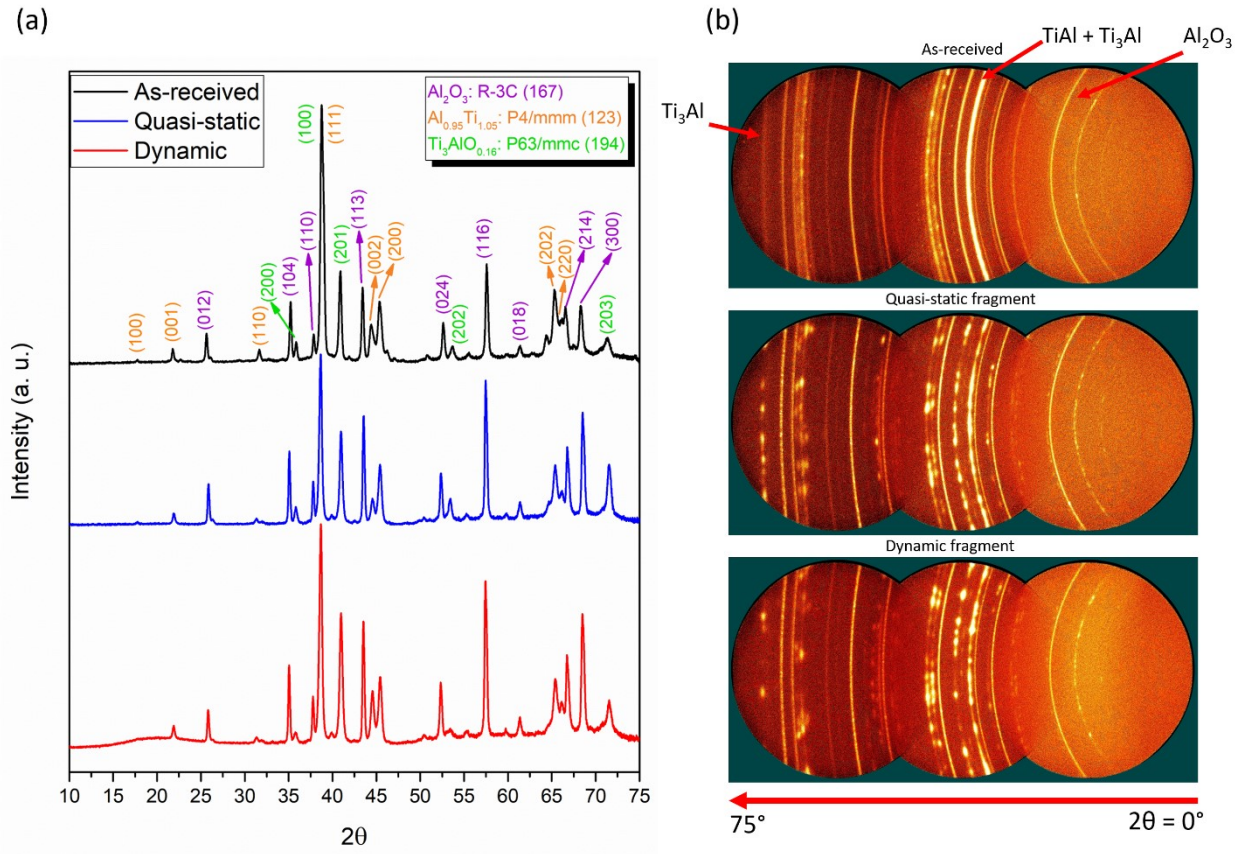

Figure 11: X-ray diffraction analysis of the as-received TiAl/Ti_3Al-Al_2O_3 cermet, and of a polished fracture surface taken from a quasi-static fragment and a dynamic fragment showing phases changes and crystallinity evolution during uniaxial compressive loading at different strain rates. (a) $\theta - 2\theta$ equivalent spectrum plots showing an amorphous peak occurs in the dynamic fragment, where no additional phase changes occur under both quasi-static and dynamic loading; (b) 2D diffraction frame revealing crystalline texturing evolves at different loading rates. The light intensity is integrated from right to left to obtain the 1-D spectrums. Typical peaks corresponding to the three phases are pointed out by red arrows to show the texturing evolution in different phases. Significant crystalline texturing is observed in the dynamic fragment on both γ-TiAl and α_2-Ti_3Al phases, whereas alumina phase remains in its randomly orientated polycrystalline structure.

5. Discussion

This paper explores the rate-dependent stress-strain responses, material properties, failure mechanisms, and crystalline texture evolution of a SHS fabricated TiAl/Ti_3Al-Al_2O_3 cermet under both quasi-static and dynamic uniaxial compression. First, mechanical tests were performed using a conventional MTS machine and modified split Hopkinson pressure bar, and novel digital image correlation was used to extract the strain data to obtain the stress-strain curves. Next, microscopic

diagnosis using SEM with EDS and TEM, and 2D-XRD were used to investigate the failure mechanisms and crystalline texturing behavior of the material observed as a consequence of mechanical loading and associated deformation. The current work builds on the framework of former WC-Co, SiC-Ti, SiC-Al, B_4C-Al, TiB_2-Al, and TiC-Steel cermet systems [5, 9, 11, 17, 46, 64 – 67] by studying the rate-dependency of material responses of these materials, as well as extends to the TiAl/Ti_3Al-Al_2O_3 cermet oxide cermet where studies have mainly focus on fabrication methods [28 – 33]. In the first sub-section of the discussion, critical observations on the rate-dependency of material properties of our cermet will be highlighted, and these values will be compared with other cermet systems. In the second sub-section of the discussion, a rate-dependency exponent and a transition strain rate of the studied TiAl/Ti_3Al-Al_2O_3 cermet will be postulated based on the compressive strength results. In this sub-section, the rate sensitivity will also be discussed based on the flow stress. In the third sub-section of the discussion, rate-dependent micro/nanoscale failure mechanisms and crystalline texturing behavior will be assessed in the current material and compared with other cermet systems. In the last sub-section of the discussion, material implications on protection applications will be emphasized based on the relevant ballistic performance metrics currently used in impact testing.

5.1 Comparing stress-strain responses to those of other cermet systems

In this sub-section, the rate-dependent stress-strain responses of the TiAl/Ti_3Al-Al_2O_3 cermet will be discussed with respect to stiffness and failure strains, and these will be emphasized by comparing to other cermet systems (e.g., SiC-Al [47], TiC-steel [67]). The strength values will be compared in the next sub-section of the Discussion. At the low and high strain rate loading, the stress-strain curves exhibit an initial linear elastic portion. In the quasi-static case (see Fig. 4), the stress increases linearly to ~ 0.002, whereas the stress increases linearly up to approximately 0.008

under dynamic loading. In the current cermet, the stiffness has an average of 267 ± 28 GPa and 255 ± 11 GPa under quasi-static and dynamic loading, respectively. First, it is observed that the offset of the linear elastic region of the dynamic stress-strain response increases from the quasi-static case by ~ 0.006 (from ~ 0.002 to ~ 0.008) in strain. In linear elastically behaving materials like ceramics, microcrack initiation, growth, and coalescence is considered the dominant failure mechanism [68]. This extended linear elastic regime of the $TiAl/Ti_3Al$-Al_2O_3 cermet under dynamic loading is attributed to the limited velocity of crack growth compared to the high strain rates [69]. In a linear elastic material with a certain stiffness, this essentially means an increase in strength and failure strain for higher strain rates when compared to quasi-static behavior [69, 70]. Second, no clear rate-dependency of the stiffness is observed in the present study. This agrees with most of the works being done on cermets, where stiffness was often reported as one of the rate insensitive properties of a material (e.g., ~ 78 GPa for a 40 vol% SiC_p-2024 Al cermet and ~ 135 GPa for a 50 vol% SiC_p-2024 Al cermet from quasi-static to 2500 s^{-1} strain rate [47], ~ 360 GPa for a group of TiC-steel cermets from quasi-static to plate impact tests [67], ~ 25 GPa for a 35 vol% Al_2O_3-Mg cermet from 10^{-4} s^{-1} to 1550 s^{-1} strain rate [71], and ~ 50 GPa for a B_4C-Al cermet from 10^{-3} s^{-1} to 2250 s^{-1} strain rate [72]). In contrast, the stress-strain curves reported by Zhu et al. [66] revealed a much higher stiffness (~ 13 GPa at 0.0007 s^{-1} strain rate and ~ 60 GPa at 1100 s^{-1} strain rate) in the TiB_2-Al cermet. The reasons behind possible rate-dependency on stiffness is not yet well understood. It is worth noting that some stiffness values measured in these literature are lower than their respective constituents, and this might be related to the challenges in measuring small strains under compression. We overcome this in this study by using high resolution cameras coupled to specialized DIC techniques.

After the initial linear portion, significant differences in the compressive stress-strain behavior of the TiAl/Ti_3Al-Al_2O_3 cermet are observed (see Fig. 4 and 5). In the quasi-static tests (Fig. 4), continuous concave-shaped stress-strain curves are obtained. Unlike the case for typical titanium aluminide alloys [73 – 75], no distinct yield point is observed in these curves. The concave shape indicates a continuous degradation of instantaneous stiffness during loading, and this can be attributed to the "softening" behavior and damage accumulation in the material [2]. Sudden catastrophic failure occurs after the peak stress is reached, and the material loses its load bearing capacity. Overall, the material behaves consistently under quasi-static compression in terms of strength deviation (with a standard deviation of 60 MPa), as well as trends in the curves. In the dynamic tests (Fig. 5), the material behaves in a much more complex manner compared to the quasi-static case. In general, each stress-strain curve consists of at least two peaks, where the first peak has the highest stress value among all tests. Between two subsequent peaks, stress relaxation (flow softening) followed by strain hardening is observed. Some literature on metallic alloys under high-rate loadings explain this alternating stress phenomenon as "alternating thermal softening and strain hardening" (e.g., 7003-T4 aluminum alloy under high strain rate impact [76]). However, it is challenging to claim thermal effects in the current study without in-situ measurements. The rate-dependency in stress-strain behavior under different loading rates have been probed in other cermet systems, emphasizing the stress behavior after the initial linear portion. For example, Guden et al. [71] investigated the rate-dependent stress-strain response of a Mg-Al_2O_3 cermet and found distinct differences in stress-strain responses before failure, where the "flow softening-hardening" phenomenon observed in our cermet was also observed under dynamic loading in their study. In addition, both Rittel et al. [17] and Zhu et al. [66] found the alternating strain hardening and softening phenomena under dynamic loading of a TiC-steel and a TiB_2-Al cermet, respectively,

where both of their materials behave in a near-linear elastic manner under quasi-static loading [67]. In their studies, the changes in the stress-strain responses were attributed to either changes in failure mechanisms or the activation of additional microstructural changes during high-rate impact [66, 67]. In the current study, the failure mechanisms and crystalline texture evolution are believed to be responsible for the changes in the stress-strain response of the TiAl/Ti_3Al-Al_2O_3 cermet, and these will be discussed in detail in sub-section 5.3.

Next, we compare the failure strains (as the final point on the stress-strain curves before the onset of cracking) of the current cermet to ceramics and other cermet systems. The failure strain of the TiAl/Ti_3Al-Al_2O_3 cermet measured in quasi-static tests has an average of 0.0166 ± 0.0017, whereas the failure strain measured in dynamic tests has an average of 0.026 ± 0.0032. An approximately 1.4 times increases is observed with a seven order increase in strain rate. The failure strains of the current cermet are much higher than most of the advanced ceramics under both loading rates (i.e., between 1.0% to 1.5% for Al_2O_3 [77 – 79] and reported as 1.29% for SiC and 0.62% for Si_3N_4 [80]). Furthermore, the failure strain of the TiAl/Ti_3Al-Al_2O_3 cermet is at the higher end among some cermet systems, such as WC-Co systems (~ 2% quasi-statically for 85% WC [15]), TiC-Ni systems (~ 1.2% quasi-statically for 70% TiC [16]), and B_4C-Al systems (~ 1.6% at 0.005 s^{-1} and ~ 3% at 2000 s^{-1} for 65% B_4C [81]). Note that the volume percentage of the ceramic phases in these cermets are all sufficiently high (> 60%). At the same time, some cermet systems with aluminum (e.g., 2024Al-TiB_2) and steel (e.g., 1080 steel-TiC) as the matrix material could reach failure strains of around 10% [17, 47, 66]. Altogether, this measurement of the rate-dependent failure strains may give us some knowledge on the improvement in dynamic fracture toughness, which could be an important parameter indicative of energy dissipation in protection applications [82].

5.2 Rate sensitivity of compressive strength and flow stress

In the current study, the quasi-static compressive strength of the $TiAl/Ti_3Al$-Al_2O_3 cermet has an average of 2780 ± 60 MPa, whereas the dynamic compressive strength has an average of 3410 ± 247 MPa, and this indicates an approximately 1.3 times increase in strength with a seven order increase in strain rate (from ~ 10^{-4} s^{-1} to ~ 10^{3} s^{-1}). Most of the works done on other cermet systems investigated the rate-dependent compressive strength and reported similar orders of increase in strength under dynamic loading. For example, Mandel et al. [64] and Zhu et al. [66] reported increases in peak compressive strength between 1.3 and 1.5 times in strength in WC-Co system (from 4370 MPa to 6660 MPa with 10^{-4} s^{-1} to 10^{3} s^{-1} strain rate) and TiB_2-Al system (from 900 MPa to 1200 MPa with 0.0007 s^{-1} to 1100 s^{-1} strain rate), respectively. Some other cermet systems were reported to have lower rate-dependency on strength. For example, Li et al. [9] reported an increase in strength of 1.2 times in the A359 Al-20 vol% SiC_P cermet from 300 MPa to 360 MPa with 10^{-4} s^{-1} to 2000 s^{-1} strain rate. In another study, Behm et al. [83] reported almost no change in strength (850 – 900 MPa) in an Al 5038-B_4C cermet with 10^{-3} s^{-1} to 4000 s^{-1} strain rate increase. In contrast, Nawale et al. [84] and Hong and Gray [85] found over a two times increase in strength in A365 Al-Al_2O_3 (from 150 MPa to 350 MPa with 100 s^{-1} to 1200 s^{-1} strain rate) and 1060 Al-Al_2O_3 (from 130 MPa to 300 MPa with 0.001 s^{-1} to 6000 s^{-1} strain rate) cermet systems. Overall, the order of increase in compressive strength of the $TiAl/Ti_3Al$-Al_2O_3 cermet is comparable to other cermet systems, whereas the magnitude of the compressive strength is much higher than all the cermet systems, where aluminum is their matrix material. The rate sensitive and high compressive strength in the $TiAl/Ti_3Al$-Al_2O_3 cermet is likely a consequence of the relative high concentration of alumina (~ 65% volume percentage) and the ultrafine-grained structured of both phases in the current cermet [72]. This is important to note, as compressive strength has been

shown to be an important factor in the ballistic impact performance in some protection applications [25].

Next, we investigate the rate sensitivity of the $TiAl/Ti_3Al$-Al_2O_3 cermet. To do this, the compressive strength of the cermet is re-visited in Figure 12 for investigating the rate-sensitivity of the strength and its corresponding transition strain rate. A power law fit is performed on the data to populate the rate-dependency exponent and transition strain rate. The fit has the form:

$$\sigma_c = a * \dot{\epsilon}^n + \sigma_{QS_{avg}} \quad (6)$$

where σ_c (MPa) is the peak compressive strength, $\dot{\epsilon}$ (s^{-1}) is the corresponding strain rate, $\sigma_{QS_{avg}}$ (MPa) is the average compressive strength measured at quasi-static condition, n (unitless) is the rate-dependency exponent, and a (unitless) is the fitted coefficient which indicates the weight of the rate-dependency term. In this case, a rate-dependency exponent of approximately n = 0.87 is postulated by visualizing the goodness of fit, and the final results are plotted in the log scale to coincide with the literature. The y-interception value ("$\sigma_{QS_{avg}}$" in the equation) is fixed to the average quasi-static compressive strength to represent the initial material strength. With an exponent of n = 0.87, the fitted coefficient "a" is nearly 1 with a R^2 value of 0.9, indicating the fit is good. In addition, a transitional strain rate between 8 x 10^1 s^{-1} and 5 x 10^2 s^{-1} is proposed based on the existing data. The proposed transitional strain rate region is indicated by a red box over the fitted curve in Figure 12.

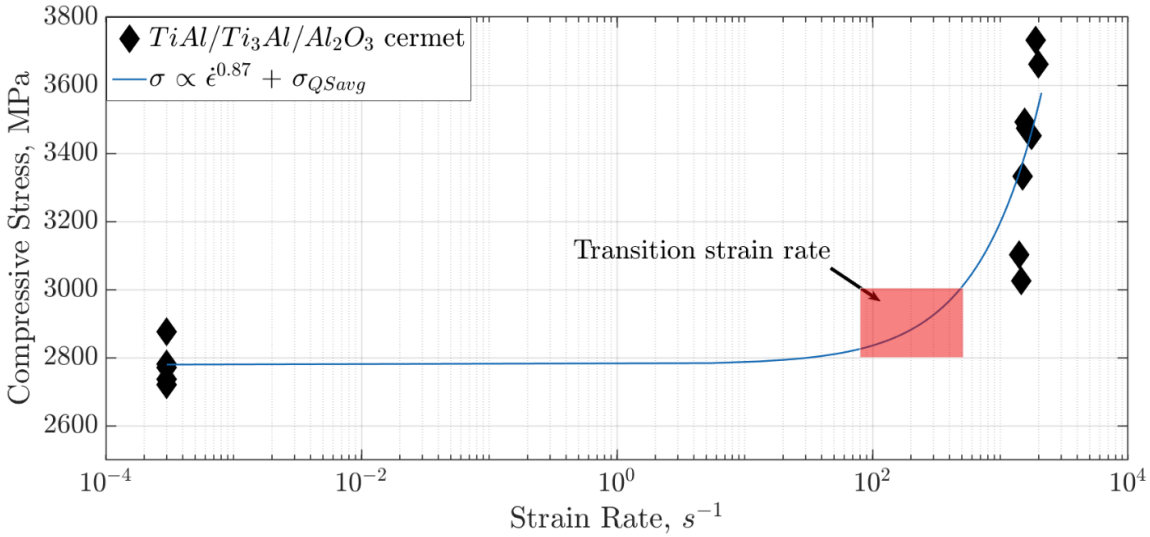

Figure 12: Summary of the compressive strength of the cermet at different strain rates (in log scale). A curve fit in the form of $\sigma_c = a * \dot{\epsilon}^n + \sigma_{QS_{avg}}$ is used to determine the rate-dependency exponent, n, for compressive strength as well as the transitional strain rate. This is evaluated to be 80 to 500 s^{-1}. This method has been used widely in studying the rate dependency of brittle materials [89, 90]. The fitted coefficient, "a" is close to 1 with a R^2 value of 0.9, indicating a good fit.

In other literature investigations on the rate-dependency of particle-reinforced MMCs, Hong et al. [86], followed by Bao and Lin [87], proposed a framework based on the work of an Al-Zn-Mg-Cu alloy reinforced with SiC cermet and concluded that the rate sensitivity of the composite was highly dependent on the matrix material. The rate sensitivity, R_s, in Hong et al. [86] and Bao and Lin's [87] work is expressed as:

$$R_s = \frac{\sigma_d - \sigma_s}{\sigma_s} \frac{1}{ln(\frac{\dot{\varepsilon_d}}{\dot{\varepsilon_s}})} \tag{7}$$

where σ_d(MPa) and σ_s (MPa) are the dynamic and quasi-static flow stresses at a constant plastic strain, respectively, and $\dot{\varepsilon_d}$ (s^{-1}) and $\dot{\varepsilon_s}$ (s^{-1}) are the corresponding strain rate. Instead of using the compressive strength (peak stress) as the reference point, flow stress at a constant plastic strain is used to determine the rate sensitivity of a material. By taking the flow stress at approximately 1.5% strain for all tests performed in the present study (after the first peak in dynamic tests), the rate sensitivity of the $TiAl/Ti_3Al$-Al_2O_3 cermet determined by using this method is between 0.025 to

0.030. This is higher than the rate sensitivity reported by Tan et al. [47] for a 50 vol.% SiC reinforced 2024 Al cermet ($R_s \sim 0.022$) and Guo et al. [88] for TiB_2-2024Al cermet ($R_s \sim 0$ at room temperature and $R_s \sim 0.01$ at 100 °C), suggesting that our material is quite rate sensitive.

The power law fitting method has been well established in the literature for investigating the rate-dependency exponent of brittle materials, and some well-known rate-dependency exponents have been proposed to model the rate sensitivity of compressive strength. For example, Lankford [89] used 1/3 as the exponent to describe the rate-dependency of the compressive strength for alumina. In another work, Kimberly [90] proposed another rate-dependency exponent as 2/3 to represent the group of brittle materials by considering crack-crack interactions under dynamic loading in a self-consistent framework. This was done under the assumption that the material would deform in the purely brittle manner (crack initiation, growth, and coalescence) with defined appropriate time scales and length scales for internal flaws and crack growth. For the $TiAl/Ti_3Al$-Al_2O_3 cermet in this study, it is believed that the rate-dependency exponent should not be bounded by these numbers because of the activation of the failure mechanisms in addition to cracking under dynamic loading. These extra energy-dissipation mechanisms, which are no longer observed in localized regions and small scales, are believed to manifest as the global "surface texturing" phenomenon under dynamic loading. The effects of extra failure mechanisms have also been noted by Lankford [91] that if the elastic expansion (kinetic) energy was no longer balanced by the pure fracture surface (potential) energy, the rate-dependency exponent could be much higher than the proposed 1/3. In a later work of Lankford [78], the rate sensitivities of a hot-pressed Si_3N_4 was found to be 0.87 at the strain rate of 10^3 s^{-1} and so values higher than 2/3 have been reported before. He concluded that this deviation from the formally proposed 1/3 rule was the consequence of localized plasticity and the suppression of local plastic flow by high loading rates. For material such as the

$TiAl/Ti_3Al$-Al_2O_3 cermet with a complicated nano-grained microstructure and combination of elastic and plastic deformation mechanisms, we found that the power law fit presented in this study (see Equation (6)) will provide a better postulate on the rate-dependency of the material. However, it is still recommended that investigations need to be done at the intermediate strain rates ($\sim 10^{-2}$ s^{-1} to $\sim 10^{2}$ s^{-1}, such as a modified servo-hydraulic technique [134]) and higher strain rates ($> 10^{4}$ s^{-1}, such as plate impact experiments [135]) to probe a boarder range of material responses.

5.3 Rate-dependent failure mechanisms and crystalline texturing behavior

In this sub-section, the rate-dependency of the $TiAl/Ti_3Al$-Al_2O_3 cermet is explored in the context of the rate-dependent failure mechanisms (i.e., inter/transgranular cracking, particle fracture, dislocation and twinning), as well as the crystalline texturing phenomenon observed through XRD and high-speed imaging. First, the microscale mechanisms, such as inter/transgranular cracking and grain boundary delamination, are examined using SEM and EDS (see Fig. 7 and 8). In summary, a high density of intergranular cracking is observed under quasi-static loading, where minimal transgranular cracking is observed on both fracture and polished fracture surfaces. In addition, grain boundary delamination and particle pull-out constitute some of the major failure mechanisms under quasi-static compression, where small amounts of cleavage are observed in the titanium aluminide phase. Under dynamic loading, the material exhibits uneven fracture planes with much denser lamellar tearing occurring in the titanium aluminide matrix (see Fig. 8-c). A combination of intergranular *and* transgranular cracking are activated simultaneously during loading, and large amounts of particle cracking is observed on the polished fracture surface. In addition, void growth is observed on the polished fracture surface under dynamic loading, and they tend to grow along or within the alumina phase (see Fig. 8-a and b). With the voids acting as the sites for stress concentration, microcracks are likely to grow by connecting these voids, and these

eventually coalescence to form localized ductile crack networks. The different mechanisms observed under low and high strain rates can be interpreted using energy accumulated in different timescales. When the material is loaded at high strain rates, higher kinetic energy and stress introduced to the material at a smaller timescale results in particle fractures being prevalent [92]. At such small timescale, transgranular cracks could initiate in the matrix and propagate through the particles, when a much higher stress level is achieved within microseconds. This is different from intergranular cracking which requires less energy to exfoliate the interfaces and larger timescale for propagating along the particles [93]. Similarly, the apparent increase in void nucleation and growth can be the result of the higher level of strain energy generated under dynamic loading in the vicinity of the particle boundaries, and this is caused by stress concentration and localized tensile stress field at the matrix-particle interface from lateral expansion [93, 94]. This is likely why most of the voids are observed at the boundary of the alumina phase (see Fig. 8-b) in the current TiAl/Ti_3Al-Al_2O_3 cermet. In addition, void growth is usually connected with interface delamination and particle pull-out, which are major failure mechanisms observed in particle reinforced MMC studies [93, 95, 96]. To integrate particle pull-out in modeling work on particle-reinforced MMCs, Needleman [94, 97] used a cohesive zone model in his works to describe the process of void nucleation through interfacial debonding and concluded on the dynamic effect of stress redistribution around the matrix-particle interface. Eventually, this global increase in void growth indicates that the TiAl/Ti_3Al-Al_2O_3 cermet behaves in a more ductile manner under dynamic loading, and therefore leads to the greater area under the stress-strain curves (see Fig. 5).

Next, the cracking behavior of the TiAl/Ti_3Al-Al_2O_3 cermet is similar to what has been observed in the TiC-1080 steel by Kaplan et al. [57], who used TEM to probe the failure mechanisms under

both quasi-static and dynamic bending. They concluded interfacial cracking with crack propagation in the steel matrix being the major mechanism in the quasi-static case, and transgranular TiC particle cracking without extension to the steel matrix as the additional mechanisms activated under dynamic loading. In other cermet studies, particle fracture under dynamic loading was also observed extensively, whereas matrix fracture and particle debonding were found commonly in quasi-static tests [47, 66, 98]. In addition, Hao et al. [99] concluded that at room temperature, the γ-based TiAl alloy they tested under dynamic compression was in a brittle shear failure owing to the rapid propagation of micro-cracks along the lamella interface. In the current study, this may explain the significantly denser cleavage observed in the titanium aluminide matrix under dynamic loading of the TiAl/Ti_3Al-Al_2O_3 cermet. In some cermet systems with aluminum being the matrix, matrix melting by adiabatic heating within the shear bands under dynamic loading was observed (e.g., 2024 Al-SiC cermet [47] and 2024 Al-TiB_2 cermet [66]), but such phenomenon is not observed in any investigated sites in the current study on the TiAl/Ti_3Al-Al_2O_3 cermet. We believed that even though shear banding is one of the deformation mechanisms that could be activated in titanium aluminide under isothermal compression [100], it is not likely to be the cause of failure under room temperature dynamic compression at ~ 10^3 s^{-1} strain rates.

Next, TEM analysis (see Fig. 10) on the fragments from dynamic experiments revealed globally-distributed dislocations and twinning in the titanium aluminide phase, with localized dislocations observed in the alumina phase. Many studies have been focused on deformation dislocations and twins in γ-based TiAl alloys and their influences in material properties [101 – 104]. For example, Appel [105] investigated deformation twinning in a Ti-(45–49)Al + (0.3–10)X alloy (X being third elements) under different deformation conditions, such as strain rates, creep, and fracture. Detailed crystallographic information has also been given on twin nucleation and propagation, boundary

structures, and interactions between dislocations and twins. In another study, Maloy and Gray [73] explored the high strain rate compressive deformation mechanisms of a Ti-48A1-2Nb-2Cr alloy under strain rates between 0.001 s^{-1} and 2000 s^{-1}. They found extensive twinning and dislocations in between and across the γ/α_2 lamellae, and their amounts increased with increasing strain rate. Other recent studies (e.g., Beran et al. [106] and Guo et al. [107]) also observed similar nanoscale twinning and dislocation activities under different mechanical loadings and temperatures, with clear rate-dependencies on their extent. This confirms the observations in the current material that dislocation and twinning are universal in titanium aluminide under high-rate loading.

Finally, crystalline texturing of the $TiAl/Ti_3Al$-Al_2O_3 cermet is studied by 2D-XRD (see Fig. 11) and confirmed with high speed video images demonstrating deformation features on the surface of the specimen during dynamic compression experiments (see Fig. 5). The 2D diffraction results reveal extensive crystalline texturing occurring in titanium aluminide under dynamic loading, while the alumina phase remains in its randomly orientated polycrystalline structure. It is believed that this crystalline texturing behavior is the consequences of dynamic recrystallization and grain reorientation in the titanium aluminide phase [108, 109], and this eventually leads to a large scale surface texturing observed in the high speed videos in dynamic tests (see Fig. 5-c). The dynamic recrystallization and grain reorientation behavior often lead to extensive microstructural evolution, and this can be asserted by comparing the as-received (see Fig. 1-c) and deformed (see Fig. 9-a) states of the material. In the $TiAl/Ti_3Al$-Al_2O_3 cermet, the titanium aluminide phase undergoes global and extensive microstructural changes (from a combination of equiaxed and randomly orientated lamellar structures to uniformly orientated and alternating γ/α_2 lamellae), and the alumina phase remains permanent for uniaxial compressive loading rates of at least up to $\sim 10^3$ s^{-1} strain rate.

Microstructural evolution and crystalline texturing have been considerably studied in titanium aluminide, due to its capacity for forming complex microstructures and their significant effects on material performance. For example, Wang et al. [101] and Wu et al. [102] investigated the dynamic recrystallization behavior of TiAl alloys during high-rate compression and found severe microstructural and crystalline texture evolution, and they were found to be closely related to dislocation and twinning activities occurring during loading. Wu et al. [102] also pointed out that the degree of crystalline texturing and dynamic recrystallization is sensitive to strains. In the TiAl/Ti_3Al-Al_2O_3 cermet in this study, as the failure strain increases with increasing strain rate, the crystalline texturing becomes more dominant and this manifests macroscopically. It is known that material properties (i.e., strength) and deformation mechanisms (i.e., dislocation) can be highly dependent on the material texturing and its related changes in the microstructure [110, 111]. The activation of dislocations and twins in the titanium aluminide phase in the current cermet can be a consequence of crystalline texturing followed by profound microstructural changes [112]. The evolution of crystalline textures is also likely the driver for the "flow softening-hardening" behavior observed in the dynamic stress-strain curves (see Fig. 5-a), and subsequently, the large variabilities in the stress-strain behavior. Studies on other cermets (e.g., Al 5083-B_4C cermet [59] and TiB_2-2024 Al cermet [88]) also found significant dynamic recrystallization and microstructural changes in the matrix (aluminum in these two studies) under high-rate compression, and they were associated with dislocations or twinning. As a result, further insights on material rate sensitivity could be gained by the additional deformation mechanisms and their magnitude with increasing strain rates on top of the commonly accepted microcracking mechanism. Therefore, it is important to study the crystalline texturing behavior in detail with specific tools (i.e., pole figures) and pinpoint its exact effects on the material behavior for this complex cermet.

5.4 Implication of the material in protection applications

In this final sub-section, implications of the experimental studies on the TiAl/Ti_3Al/ Al_2O_3 cermet for protection applications, such as body armor, will be evaluated by highlighting some major ballistic performance metrics. The importance of incorporating rate-dependent mechanical properties and material behaviors for better ballistic performance prediction will be emphasized. Material improvements on ballistic performance from the material science perspectives will be underscored as well.

The ballistic performance of an armor material is generally considered from the perspective of some commonly defined criteria, such as ballistic efficiency, ballistic limit (V50), and ballistic energy dissipation capacity (the *D*-criterion). The frequently used ballistic efficiency index-differential efficiency factor (DEF) is defined as [113]:

$$DEF = \frac{(P_0 - P_r) * \rho_0}{(t_c * \rho_c)} \tag{8}$$

where P_0 (m) and P_r (m) are the reference and residual penetration of projectile in backing rolled homogeneous armor (RHA), respectively; t_c (m) denotes the ceramic target thickness; and ρ_0 (kg/m^3) and ρ_t (kg/m^3) denote the density of RHA and ceramic target, respectively. This is one of the simplest criteria in evaluating ballistic performance, where only tile geometry and depth of penetration are often considered [114]. To evaluate the effectiveness of a material using this metric along for material improvement is tedious in that it requires significant amounts of expensive testing and does not provide any guidelines in the direction of material improvement.

Next, in the National Institute of Justice (NIJ) standard-0101.06 [115], the ballistic limit is defined as the velocity at which the projectile is expected to penetrate the armor at least 50% of the times for a given bullet type. Numerous empirical equations have been developed for specific materials

or systems to better predict their ballistic limits. These expressions seek to tie critical mechanical properties to ballistic performance. For instance, Villanueva and Cantwell [116] developed the well-known expression for composite laminates:

$$V_{50\_laminate} = \frac{\pi\Gamma\sqrt{\rho_t * \sigma_e}D^2T}{4m}\left[1 + \sqrt{1 + \frac{8m}{\pi\Gamma^2\rho_t D^2 T}}\right] \quad (9)$$

where Γ (unitless) is the projectile constant; ρ_t (kg/m^3) is the density of the laminate target; σ_e (Pa) denotes the quasi-static compressive strength of the target; D (m) denotes the diameter of the projectile; T (m) is the thickness of the projectile and m (kg) is the mass of the projectile. In this case, the quasi-static compressive strength is considered by Villanueva and Cantwell [116] as the most important parameter in ballistic performance of one laminate tile. No specific expression on estimating the ballistic limit for ceramics or cermet systems has yet being developed. However, considering only the quasi-static compressive strength does not appear to be a good indication of the material capacity in stopping the projectile during an impact event given the clear rate-dependency observed on the compressive strength for most of the ceramics and cermets, in this study the TiAl/Ti_3Al-Al_2O_3 cermet. More attention is needed to incorporate the rate sensitivity of the material into the metric for more accurate prediction [82, 117]. In other works, for example, Lankford [78] emphasized the role of the dynamic mechanical properties for ceramic armor and deduced the relationship between the fragmentation behavior of the materials and strain rate dependent fracture mechanisms, as well as the inertial confinement generated under high-rate loading. In the current study for the TiAl/Ti_3Al-Al_2O_3 cermet, finding an appropriate way to incorporate the rate-sensitive mechanical properties into some metrics, such as compressive strength and failure strain, will be critical in more accurately predicting the material performance under impact.

Next, Neshpor et al. [118] proposed the term ballistic energy dissipation ability (D-criterion) for ceramic armors:

$$D = \frac{0.36(HV * E * c)}{K_{1c}^2} \tag{10}$$

where HV (MPa) is the Vickers hardness; E (MPa) is the Young's modulus (stiffness); c (m/s) is the sound velocity in the material and can be approximated by $\sqrt{\frac{E}{\rho}}$; and K_{Ic} ($\mathrm{MPa \cdot m^{1/2}}$) is the fracture toughness. More fundamental material properties are incorporated into this metric for advanced ceramics, and this is shown to give a more accurate prediction on the ballistic performance based on the understanding of the dwell (hardness and stiffness dependent) and penetration phases (fracture toughness dependent) occur during a ballistic impact event [79]. Eq. (10) indicates that a trade-off must be made between the dwell and penetration properties (i.e., hardness and stiffness in the numerator and fracture toughness in the denominator). One of the limiting factors in using advanced ceramics in protection applications is their sacrifice in fracture toughness to achieve high hardness for projectile defeat [119 – 122]. Instead, one of the major goals in cermet research is to introduce certain amounts of ductility into ceramics by incorporating a metallic phase, an intermetallic phase in the case of the TiAl/Ti_3Al-Al_2O_3 cermet, so that this results in an increase on the capacity of energy dissipation during projectile penetration [4]. For the TiAl/Ti_3Al-Al_2O_3 studied in this work, the increase in failure strains when compared to other advanced ceramics indicates an increase in ductility and fracture toughness, while maintaining a comparable compressive strength with some of the advanced ceramics (e.g., alumina [38]). The combination of higher failure strains and comparable compressive strength provides some knowledge on the increase in fracture toughness. In addition, the 1.4 times increase in failure strain and the 1.3 times increase in compressive strength under dynamic loading in the current cermet

results in significantly higher dynamic fracture toughness than that of its quasi-static counterpart. Similar results have been shown in other cermet systems (e.g., ~ 3 times increase in fracture toughness in a TiC-1080 steel cermet from quasi-static to dynamic bending tests [17]). Unlike other cermet systems with aluminum or steel being the matrices, the intermetallic titanium aluminide in the current cermet system preserves a much higher strength and stiffness (i.e., < 1.2 GPa in compressive strength for Al-based cermets [72, 84, 123]), which are critical properties in ballistic performance.

Overall, metrics of ballistic performance are represented by either critical mechanical properties, such as density, stiffness, compressive strength, hardness, and fracture toughness, or armor system variables, such as tile thickness, tile geometry, and projectile information. From a material science perspective, more focus is dedicated to improving the mechanical properties of one material, essentially, finding the optimized microstructure (i.e., phase compositions, grain size and shape, secondary reinforcements) [30, 125 – 128]. For example, Landingham and Casey [129] provided proof of an optimal phase composition for a TiC-based (Ni, Mo) enhanced cermet in terms of ballistic limit performance. At about 10 vol% of (Ni, Mo) metallic phases, the ballistic limit (V50) could reach 3100 ft/s, which is 20% higher than pure TiC ceramic and 7% higher than the material containing 33 vol% of (Ni, Mo) metallic phases. In the case of the $TiAl/Ti_3Al$-Al_2O_3 cermet in this study, controlling the phase composition by tailoring the initial powders, adding alloying elements, and changing the microstructure by heat treatments is expected to result in notable changes in material properties. Specifically, tailoring the microstructure of the titanium aluminide phase to reduce the effect of crystalline texturing is believed to alter the flow stress softening and, perhaps, deliver better performances under impact [58, 112, 130]. In addition, fragmentation behavior of the target material, which has an influence on projectile erosion [79], is worth studying in length.

According to numerous studies, fragmentation will likely be affected by the microstructure, and hence the fracture mechanisms [78, 131, 132]. It is concluded that the cermet materials need to be systematically studied before they can ultimately replace the role of advanced ceramics, such as alumina in protection applications.

6. Conclusion

In this study, the rate-dependency of a SHS-synthesized TiAl/Ti_3Al-Al_2O_3 cermet was investigated using mechanical testing and advanced microscopy. Quasi-static and dynamic uniaxial compression tests coupled with high-speed imaging and DIC were performed to assess the rate-dependent mechanical responses, including stress-strain behavior, compressive strength, failure strain, and macroscopic failure, and these were compared with other advanced ceramics and cermet systems. The TiAl/Ti_3Al-Al_2O_3 cermet exhibited the "flow hardening-softening" phenomenon under dynamic loading with increased compressive strengths and failure strains when compared with the quasi-static counterpart. In addition, the current material had a much higher magnitude of compressive strength than most of the aluminum-based cermets while maintaining a comparable order of increase with increasing strain rates. A rate-dependency exponent of 0.87 was proposed to capture the rate sensitivity of the peak compressive strength. Advanced characterization, including SEM, HR-TEM, 2D-XRD were used to explore the rate-dependency in failure mechanisms of the current material, where globally distributed dislocations and twinning were observed under dynamic loading. Extensive cleavage in the TiAl phase, void growth, transgranular cracking, and particle fracture were identified as the main failure mechanisms under high strain rates. Crystalline texturing behavior in the TiAl phase was identified by 2D-XRD, where extensive microstructural evolution with grain reorientation and dynamic recrystallization was observed under TEM. The post-deformed TiAl phase reveals a fully lamellar structure with alternating γ/α_2

lamellae. This microscopic texturing behavior eventually manifested as the macroscopic surface texturing observed under dynamic loading using high-speed imaging. Altogether, this study delivers a comprehensive understanding on the rate-dependent mechanical properties and failure mechanisms of the $TiAl/Ti_3Al$-Al_2O_3 cermet. Furthermore, the data generated in this study provides insights in cermet material micromechanical modeling and optimization.

Acknowledgements

This research was sponsored by the Natural Sciences and Engineering Research Council of Canada (Grant #2016-04685) with support from PRE Labs Inc. and Lumiant Corporation. We thank Calvin Lo and Bernie Faulker for aiding in the completing the experiments.

Data Availability

- The raw/processed data required to reproduce these findings cannot be shared at this time due to technical or time limitations.
- The raw/processed data required to reproduce these findings cannot be shared at this time as the data also forms part of an ongoing study.

Reference

[1] Pickering, E. G., et al. "Effect of confinement on the static and dynamic indentation response of model ceramic and cermet materials." *International Journal of Impact Engineering* 110 (2017): 123-137.

[2] San Marchi, C., et al. "Quasistatic and dynamic compression of aluminum-oxide particle reinforced pure aluminum." *Materials Science and Engineering: A* 337.1-2 (2002): 202-211.

[3] Li, Yulong, K. T. Ramesh, and E. S. C. Chin. "Comparison of the plastic deformation and failure of A359/SiC and 6061-T6/Al2O3 metal matrix composites under dynamic tension." *Materials Science and Engineering: A* 371.1-2 (2004): 359-370.

[4] Wilkins, M. L., C. F. Cline, and C. A. Honodel. *FOURTH PROGRESS REPORT OF LIGHT ARMOR PROGRAM*. No. UCRL-50694. California Univ., Livermore. Lawrence Radiation Lab., 1969.

[5] Blumenthal, W. R., G. T. Gray, and T. N. Claytor. "Response of aluminium-infiltrated boron carbide cermets to shock wave loading." *Journal of Materials Science* 29.17 (1994): 4567-4576.

[6] Schwarzkopf, Paul, and Richard Kieffer. Refractory hard metals: borides, carbides, nitrides, and silicides; the basic constituents of cemented hard metals and their use as high-temperature materials. Macmillan, 1953.

[7] Ettmayer, Peter. "Hardmetals and cermets." *Annual Review of Materials Science* 19.1 (1989): 145-164.

[8] Mari, D. "Cermets and hardmetals." (2014).

[9] Li, Y., K. T. Ramesh, and E. S. C. Chin. "Viscoplastic deformations and compressive damage in an A359/SiCp metal–matrix composite." *Acta materialia* 48.7 (2000): 1563-1573.

[10] Compton, B. G., and F. W. Zok. "Impact resistance of TiC-based cermets." *International Journal of Impact Engineering*62 (2013): 75-87.

[11] Jewell, P., et al. "Rate and microstructure influence on the fracture behavior of cemented carbides WC-Co and WC-Ni." *International Journal of Fracture* 208.1-2 (2017): 203-219.

[12] Karamis, M. B., F. Nair, and A. Tasdemirci. "Analyses of metallurgical behavior of Al–SiCp composites after ballistic impacts." *Composite structures* 64.2 (2004): 219-226.

[13] Travitzky (2012) Processing of ceramic–metal composites, *Advances in Applied Ceramics*, 111:5-6, 286-300, DOI: 10.1179/1743676111Y.0000000073

[14] Taya, Minoru, and Richard J. Arsenault. *Metal matrix composites: thermomechanical behavior*. Elsevier, 2016.

[15] Johnson Jr, Aldie E. "Mechanical properties at room temperature of four cermets of tungsten carbide with cobalt binder." (1954).

[16] Kerper, Matthew J., et al. "Evaluation of tensile, compressive, torsional, transverse, and impact tests and correlation of results for brittle cermets." *Journal of Research of the National Bureau of Standards* 61.3 (1958): 149.

[17] Rittel, D., N. Frage, and M. P. Dariel. "Dynamic mechanical and fracture properties of an infiltrated TiC-1080 steel cermet." *International journal of solids and structures* 42.2 (2005): 697-715.

[18] Ramesh, K. T., and G. Ravichandran. "Dynamic behavior of a boron carbide aluminum cermet: experiments and observations." *Mechanics of Materials* 10.1-2 (1990): 19-29.

[19] Crouch, Ian G. “Body Armour – New Materials, New Systems.” *Defence Technology*, Elsevier Ltd, 2019, doi:10.1016/j.dt.2019.02.002.

[20] Meier, G. H., et al. "Environmental behaviour of intermetallic materials." S*tructural Intermetallics*, R. Darolia, J Lewandowski, CT Liu, PL Martin, DB Miracle, MV Nathal (editors), TMS, Warrendale 861 (1993).

[21] Liang, Yongfeng, and Junpin Lin. "Fabrication and Properties of γ-TiAl Sheet Materials: A Review." *JOM*, vol. 69, no. 12, 2017, pp. 2571–75, doi:10.1007/s11837-017-2551-z.

[22] Djanarthany, S., J-C. Viala, and J. Bouix. "An overview of monolithic titanium aluminides based on Ti3Al and TiAl." *Materials chemistry and physics* 72.3 (2001): 301-319.

[23] Appel, F., and R. Wagner. "Microstructure and deformation of two-phase γ-titanium aluminides." *Materials science and engineering: r: reports* 22.5 (1998): 187-268.

[24] "Advanced-Alumina-Brochure." Coorstek. Inc, 2016. https://www.coorstek.com/media/1715/advanced-alumina-brochure.pdf

[25] Rosenberg, Zvi, and Erez Dekel. *Terminal ballistics*. Berlin: Springer, 2012.

[26] Weeks, Carrell Elizabeth. Evaluation of a gamma titanium aluminide for hypersonic structural applications. Diss. Georgia Institute of Technology, 2005.

[27] Levashov, E. A., et al. "Self-propagating high-temperature synthesis of advanced materials and coatings." *International Materials Reviews* 62.4 (2017): 203-239.

[28] Cai, Z. H., and D. L. Zhang. "Sintering behaviour and microstructures of Ti (Al, O)/Al2O3, Ti3Al (O)/Al2O3 and TiAl (O)/Al2O3 in situ composites." *Materials Science and Engineering: A* 419.1-2 (2006): 310-317.

[29] Taotao, Ai. "Microstructure and mechanical properties of in-situ synthesized Al2O3/TiAl composites." *Chinese Journal of Aeronautics* 21.6 (2008): 559-564.

[30] Gaus, Shaun P., et al. "Alumina–Aluminide Alloys (3A) Technology: II, Modeling of TixAly–Al2O3 Composites Formation." *Journal of the American ceramic society* 83.7 (2000): 1606-1612.

[31] Kamali, Ali Reza, et al. "Production of TiAl (Ti3Al)/Al2O3 Nanocomposite." *Journal of Nano Research*. Vol. 3. Trans Tech Publications, 2008.

[32] Forouzanmehr, N., F. Karimzadeh, and M. H. Enayati. "Synthesis and characterization of TiAl/α-Al2O3 nanocomposite by mechanical alloying." *Journal of Alloys and Compounds* 478.1-2 (2009): 257-259.

[33] Shen, Y. F., et al. "Properties and electronic structures of titanium aluminides–alumina composites from in-situ SHS process." *Materials Science and Engineering: A* 528.4-5 (2011): 2100-2105.

[34] Lapin, J., L. Ondrúš, and O. Bajana. "Effect of Al2O3 particles on mechanical properties of directionally solidified intermetallic Ti–46Al–2W–0.5 Si alloy." *Materials Science and Engineering: A* 360.1-2 (2003): 85-95.

[35] Claussen, N., D. E. Garcia, and R. Janssen. "Reaction sintering of alumina-aluminide alloys (3A)." Journal of materials research 11.11 (1996): 2884-2888.

[36] Zhu, Jian Feng, Ji Qiang Gao, and Fen Wang. "Reaction Synthesis of TiAl-Al2O3 Composite." Key Engineering Materials. Vol. 336. Trans Tech Publications, 2007.

[37] Travitzky, N., I. Gotman, and N. Claussen. "Alumina–Ti aluminide interpenetrating composites: microstructure and mechanical properties." *Materials Letters* 57.22-23 (2003): 3422-3426.

[38] Li, H. Y., P. Motamedi, and J. D. Hogan. "Characterization and mechanical testing on novel (γ+ α2)–TiAl/Ti3Al/Al2O3 cermet." *Materials Science and Engineering: A* 750 (2019): 152-163.

[39] Farbaniec, L., et al. "Damage evolution of hot-pressed boron carbide under confined dynamic compression." *International Journal of Impact Engineering* 99 (2017): 75-84.

[40] "Global Scientific Services | We Know How." *EAG Laboratories*, www.eag.com/.

[41] P. Motamedi, K. Bosnick, K. Cadien and J. D. Hogan, *Adv. Mater. Interfaces*, 2018, 1800957, 1800957.

[42] P. Motamedi, K. Bosnick, K. Cui, K. Cadien and J. D. Hogan, *ACS Appl. Mater. Interfaces*, 2017, 9, 24722−24730.

[43] Kolsky, H., 1963. *Stress Waves in Solids*. Dover Publications, New York.

[44] Staehler, James M., et al. "Testing of high-strength ceramics with the split Hopkinson pressure bar." *Journal of the American Ceramic Society* 76.2 (1993): 536-538.

[45] Swab, Jeffrey J., et al. "Static and dynamic compression strength of hot-pressed boron carbide using a dumbbell-shaped specimen." *Journal of Materials Science* 52.17 (2017): 10073-10084.

[46] Bin, L. I. U., et al. "Compressive behavior of high particle content B4C/Al composite at elevated temperature." *Transactions of Nonferrous Metals Society of China* 23.10 (2013): 2826-2832.

[47] Tan, Z. H., et al. "The compressive properties of 2024Al matrix composites reinforced with high content SiC particles at various strain rates." *Materials Science and Engineering: A*489.1-2 (2008): 302-309.

[48] Hu, Guangli, et al. "The compressive failure of aluminum nitride considered as a model advanced ceramic." *Journal of the Mechanics and Physics of Solids* 59.5 (2011): 1076-1093.

[49] Pan, Bing, et al. "Two-dimensional digital image correlation for in-plane displacement and strain measurement: a review." *Measurement science and technology* 20.6 (2009): 062001.

[50] Schreier, Hubert, Jean-José Orteu, and Michael A. Sutton. *Image correlation for shape, motion and deformation measurements: Basic concepts, theory and applications*. Vol. 1. Boston, MA: Springer-Verlag US, 2009.

[51] Khoo, Sze-Wei, et al. “A Review of Surface Deformation and Strain Measurement Using Two-Dimensional Digital Image Correlation.” *Metrology and Measurement Systems*, vol. 23, no. 3, Jan. 2016, doi:10.1515/mms-2016-0028.

[52] Vic-2D, Correlated Solutions Inc., Irmo, South Carolina. URL ⟨http:// correlatedsolutions.com/vic-2d/⟩.

[53] Sutton, Michael A., et al. "The effect of out-of-plane motion on 2D and 3D digital image correlation measurements." *Optics and Lasers in Engineering* 46.10 (2008): 746-757.

[54] Lionello, Giacomo & Cristofolini, Luca. (2014). A practical approach to optimizing the preparation of speckle patterns for digital-image correlation. *Measurement Science and Technology.* 25. 107001. 10.1088/0957-0233/25/10/107001.

[55] Jerabek, Michael, Zoltan Major, and Reinhold W. Lang. "Strain determination of polymeric materials using digital image correlation." *Polymer Testing* 29.3 (2010): 407-416.

[56] Pan, B. (2013). Bias error reduction of digital image correlation using Gaussian pre-filtering. *Optics and Lasers in Eng.*, 51(10), 1161−1167.

[57] Kaplan, W. D., et al. "Static and dynamic mechanical damage mechanisms in TiC-1080 steel cermets." *Scripta materialia*51.1 (2004): 37-41.

[58] Li, Wei, et al. "Texture evolution, phase transformation mechanism and nanohardness of selective laser melted Ti-45Al-2Cr-5Nb alloy during multi-step heat treatment process." *Intermetallics* 85 (2017): 130-138.

[59] Li, Y., et al. "Investigation of aluminum-based nanocomposites with ultra-high strength." *Materials Science and Engineering: A* 527.1-2 (2009): 305-316.

[60] Lapin, J., T. Pelachová, and O. Bajana. "High temperature deformation behaviour and microstructure of cast in-situ TiAl matrix composite reinforced with carbide particles." *Journal of Alloys and Compounds* 797 (2019): 754-765.

[61] Domnich, Vladislav, et al. "Boron carbide: structure, properties, and stability under stress." *Journal of the American Ceramic Society* 94.11 (2011): 3605-3628.

[62] Eshchenko, R. N., et al. "Structural transformations in the deuterium-containing intermetallic compound (Ti3Al) D1.2 induced by high-pressure torsion." *The Physics of Metals and Metallography* 107.6 (2009): 594-600.

[64] Mandel, Kristin, Markus Radajewski, and Lutz Krüger. "Strain-rate dependence of the compressive strength of WC–Co hard metals." *Materials Science and Engineering: A* 612 (2014): 115-122.

[65] Wang, B. P., et al. "Strain rate-dependent compressive deformation and failure behavior of porous SiC/Ti-based metallic glass composite." *Materials Science and Engineering: A* 609 (2014): 53-59.

[66] Zhu, Dezhi, et al. "Dynamic deformation behavior of a high reinforcement content TiB2/Al composite at high strain rates." *Materials Science and Engineering: A* 487.1-2 (2008): 536-540.

[67] Klein, B., et al. "Dynamic response of ceramic-metal composites: The TiC-Steel system." *Journal of applied physics* 93.2 (2003): 968-976.

[68] Ashby, M. F., and C. G. Sammis. "The damage mechanics of brittle solids in compression." *Pure and Applied Geophysics*133.3 (1990): 489-521.

[69] Holland, Chance C., and Robert M. McMeeking. "The influence of mechanical and microstructural properties on the rate-dependent fracture strength of ceramics in uniaxial compression." *International Journal of Impact Engineering* 81 (2015): 34-49.

[70] Johnson, Gordon R., Timothy J. Holmquist, and Stephen R. Beissel. "Response of aluminum nitride (including a phase change) to large strains, high strain rates, and high pressures." *Journal of Applied Physics* 94.3 (2003): 1639-1646.

[71] Güden, Mustafa, et al. "Effect of strain rate on the compressive mechanical behavior of a continuous alumina fiber reinforced ZE41A magnesium alloy based composite." *Materials Science and Engineering: A* 425.1-2 (2006): 145-155.

[72] Vogt, R., et al. "High strain rate deformation and resultant damage mechanisms in ultrafine-grained aluminum matrix composites." *Materials Science and Engineering: A* 527.21-22 (2010): 5990-5996.

[73] Maloy, S. A., and G. T. Gray III. High strain rate deformation of Ti-48Al-2Cr-2Nb in the duplex morphology. No. LA-UR-95-739; CONF-950201-15. Los Alamos National Lab., NM (United States), 1995.

[74] Semiatin, S. L., et al. "Plastic-flow behavior and microstructural development in a cast alpha-two titanium aluminide." Metallurgical Transactions A 23.1 (1992): 295-305.

[75] Zeng, Shangwu, et al. "Flow behavior and processing maps of Ti-44.5 Al-3.8 Nb-1.0 Mo-0.3 Si-0.1 B alloy." *Journal of Alloys and Compounds* 698 (2017): 786-793.

[76] Wu, Xiaodong, et al. "Development of adiabatic shearing bands in 7003-T4 aluminum alloy under high strain rate impacting." *Materials Science and Engineering: A* 732 (2018): 91-98.

[77] Luo, Huiyang, and Weinong Chen. "Dynamic compressive response of intact and damaged AD995 alumina." *International Journal of Applied Ceramic Technology* 1.3 (2004): 254-260.

[78] Lankford Jr, James. "The role of dynamic material properties in the performance of ceramic armor." *International Journal of Applied Ceramic Technology* 1.3 (2004): 205-210.

[79] Krell, Andreas, and Elmar Strassburger. "Order of influences on the ballistic resistance of armor ceramics and single crystals." *Materials Science and Engineering: A* 597 (2014): 422-430

[80] Jiao, T., et al. "High rate response and dynamic failure of structural ceramics." *International Journal of applied ceramic technology* 1.3 (2004): 243-253.

[81] Blumenthal, William R. "High strain rate compression testing of ceramics and ceramic composites." *Advances in Ceramic Armor: A Collection of Papers Presented at the 29th International Conference on Advanced Ceramics and Composites*, Jan 23-28, 2005, Cocoa Beach, FL. Vol. 296. John Wiley & Sons, 2009.

[82] Chen, Weinong W., et al. "Dynamic fracture of ceramics in armor applications." *Journal of the American Ceramic Society*90.4 (2007): 1005-1018.

[83] Behm, Nathan, et al. "Quasi-static and high-rate mechanical behavior of aluminum-based MMC reinforced with boron carbide of various length scales." *Materials Science and Engineering: A* 650 (2016): 305-316.

[84] Nawale, S. P., R. T. Vyavahare, and A. S. Aradhye. "High Strain Rate Response of A356/Al2O3 Aluminum Alloy MMCs Using Ls-Dyna." *Procedia Engineering* 173 (2017): 1967-1974.

[85] Hong, S. I., and G. T. Gray. "Dynamic mechanical response of a 1060 Al/Al2O3 composite." *Journal of materials science*29.11 (1994): 2987-2992.

[86] Hong, S. I., G. T. Gray III, and J. J. Lewandowski. "Dynamic deformation behavior of Al-Zn-Mg-Cu alloy matrix composites reinforced with 20 Vol.% SiC." *Acta metallurgica et materialia* 41.8 (1993): 2337-2351.

[87] Bao, G., and Z. Lin. "High strain rate deformation in particle reinforced metal matrix composites." *Acta materialia* 44.3 (1996): 1011-1019.

[88] Guo, Q., et al. "SEM and TEM characterization of the microstructure of post-compressed TiB2/2024Al composite." *Micron* 43.2-3 (2012): 380-386.

[89] Lankford, J. "Mechanisms Responsible for Strain-Rate-Dependent Compressive Strength in Ceramic Materials." *Journal of the American Ceramic Society* 64.2 (1981): C-33.

[90] Kimberley, J., K. T. Ramesh, and N. P. Daphalapurkar. "A scaling law for the dynamic strength of brittle solids." *Acta Materialia* 61.9 (2013): 3509-3521.

[91] Lankford, J. A. M. E. S., and C. R. Blanchard. "Fragmentation of brittle materials at high rates of loading." *Journal of materials science* 26.11 (1991): 3067-3072.

[92] Finot, M., et al. "Micromechanical modeling of reinforcement fracture in particle-reinforced metal-matrix composites." *Metallurgical and Materials Transactions A* 25.11 (1994): 2403-2420.

[93] Basak, A. K., Alokesh Pramanik, and Mohammad Nazrul Islam. "Failure mechanisms of nanoparticle reinforced metal matrix composite." *Advanced Materials Research*. Vol. 774. Trans Tech Publications, 2013.

[94] Needleman, Alan. "A continuum model for void nucleation by inclusion debonding." *Journal of applied mechanics* 54.3 (1987): 525-531.

[95] Ai, Taotao, et al. "Microstructural and mechanical properties of dual Ti3AlC2–Ti2AlC reinforced TiAl composites fabricated by reaction hot pressing." *Ceramics International* 40.7 (2014): 9947-9953.

[96] Zhang, H., K. T. Ramesh, and E. S. C. Chin. "Effects of interfacial debonding on the rate-dependent response of metal matrix composites." *Acta materialia* 53.17 (2005): 4687-4700.

[97] Needleman, A. "An analysis of decohesion along an imperfect interface." *Non-Linear Fracture*. Springer, Dordrecht, 1990. 21-40.

[98] Lee, Hyungsoo, et al. "Effects of SiC particulate size on dynamic compressive properties in 7075-T6 Al-SiCp composites." *Materials Science and Engineering: A* 738 (2018): 412-419.

[99] Yanjun, Hao, et al. "Investigation on dynamic properties and failure mechanisms of Ti–47Al–2Cr–2Nb alloy under uniaxial dynamic compression at a temperature range of 288 K–773 K." *Journal of Alloys and Compounds* 649 (2015): 122-127.

[100] Cui, Ning, et al. "Hot deformation behavior and dynamic recrystallization of a β-solidifying TiAl alloy." *Materials Science and Engineering: A* 652 (2016): 231-238.

[101] Wang, Bingfeng, et al. "Mechanical properties and microstructure in a fine grained Ti-5Al-5Mo-5V-1Cr-1Fe titanium alloy deformed at a high strain rate." *Materials Science and Engineering: A* 736 (2018): 202-208.

[102] Wu, Yang, et al. "Dynamic recrystallization and texture evolution of Ti-22Al-25Nb alloy during plane-strain compression." *Journal of Alloys and Compounds* 749 (2018): 844-852.

[103] Simkin, B. A., et al. "Crack opening due to deformation twin shear at grain boundaries in near-γ TiAl." *Intermetallics* 15.1 (2007): 55-60.

[104] Edwards, Thomas Edward James, et al. "Deformation of lamellar TiAl alloys by longitudinal twinning." *Scripta Materialia*118 (2016): 46-50.

[105] Appel, F. "An electron microscope study of mechanical twinning and fracture in TiAl alloys." *Philosophical Magazine*85.2-3 (2005): 205-231.

[106] Beran, Premysl, et al. "Complex investigation of deformation twinning in γ-TiAl by TEM and neutron diffraction." *Journal of the Mechanics and Physics of Solids* 95 (2016): 647-662.

[107] Guo, Wenqi, et al. "Nanoscale Twinned Ti-44Al-4Nb-1.5 Mo-0.007 Y Alloy Promoted by High Temperature Compression with High Strain Rate." *Metals* 8.8 (2018): 619.

[108] Humphreys, Frederick John, and Max Hatherly. *Recrystallization and related annealing phenomena*. Elsevier, 2012.

[109] Huang, K., and R. E. Logé. "A review of dynamic recrystallization phenomena in metallic materials." *Materials & Design* 111 (2016): 548-574.

[110] Randle, Valerie, and Olaf Engler. *Introduction to texture analysis: macrotexture, microtexture and orientation mapping*. CRC press, 2014.

[111] Kocks, U. Fred, et al. *Texture and anisotropy: preferred orientations in polycrystals and their effect on materials properties*. Cambridge university press, 2000.

[112] Sankaran, A., et al. "Texture and microstructure evolution during tempering of gamma-massive phase in a TiAl-based alloy." *Intermetallics* 17.12 (2009): 1007-1016.

[113] Huang, Feng-Lei, and Lian-Sheng Zhang. "Investigation on ballistic performance of armor ceramics against long-rod penetration." *Metallurgical and Materials Transactions A* 38.12 (2007): 2891-2895.

[114] Savio, S. G., et al. "An experimental study on ballistic performance of boron carbide tiles." *International Journal of Impact Engineering* 38.7 (2011): 535-541.

[115] Mukasey, M. B., J. L. Sedgwick, and D. W. Hagy. "Ballistic Resistance of Body Armor, NIJ Standard-0101.06." *US Department of Justice (www. ojp. usdoj. gov/nij)* (2008).

[116] Villanueva, G. Reyes, and W. J. Cantwell. "The high velocity impact response of composite and FML-reinforced sandwich structures." *Composites Science and Technology* 64.1 (2004): 35-54.

[117] Rozenberg, Z., and Y. Yeshurun. "The relation between ballistic efficiency and compressive strength of ceramic tiles." *International journal of impact engineering* 7.3 (1988): 357-362.

[118] Neshpor, V. C., G. P. Zaitsev, and A. L. Maystrenko. "Armour ceramics ballistic efficiency evaluation." *Abstr. of 8th CIMTEC World Ceramics Congress Forum New Materials (Florencia, Italy)*. –1994.–P. Vol. 102. 1994.

[119] Launey, Maximilien E., and Robert O. Ritchie. "On the fracture toughness of advanced materials." *Advanced Materials* 21.20 (2009): 2103-2110.

[120] Quinn, George D., et al. "Fracture toughness of advanced ceramics at room temperature." *Journal of research of the National Institute of Standards and Technology* 97.5 (1992): 579.

[121] Silva, M. V., et al. "Alumina-based ceramics for armor application: mechanical characterization and ballistic testing." *Journal of Ceramics* 2014 (2014).

[122] Yang, Mijia, and Pizhong Qiao. "High energy absorbing materials for blast resistant design." *Blast Protection of Civil Infrastructures and Vehicles Using Composites*. Woodhead Publishing, 2010. 88-119.

[123] Alizadeh, Ali, Mohammad Maleki, and Alireza Abdollahi. "Preparation of super-high strength nanostructured B4C reinforced Al-2Cu aluminum alloy matrix composites by mechanical milling and hot press method: microstructural, mechanical and tribological characterization." *Advanced Powder Technology* 28.12 (2017): 3274-3287.

[124] Pötschke, J., et al. "Grain growth inhibition in ultrafine hardmetals." *International Journal of Refractory Metals and Hard Materials* 66 (2017): 95-104.

[125] Liu, N., et al. "Microstructure, hardness and fracture toughness of TiC based cermets with nano TiN powders addition." *Powder metallurgy* 50.2 (2007): 142-147.

[126] Gopal Krishna, U. B., K. V. Sreenivas Rao, and B. Vasudeva. "Effect of boron carbide reinforcement on aluminium matrix composites." *International Journal of Metallurgical & Materials Science and Engineering (IJMMSE) ISSN* (2013): 41-48.

[127] Joardar, J., S. W. Kim, and S. Kang. "Effect of nanocrystalline binder on the microstructure and mechanical properties of ultrafine Ti (CN) cermets." *Materials Science and Engineering: A* 360.1-2 (2003): 385-389.

[128] Zheng, Yong, et al. "Effect of nano addition on the microstructures and mechanical properties of Ti (C, N)-based cermets." *Ceramics International* 31.1 (2005): 165-170.

[129] Landingham, R. L., and A. W. Casey. *Final report of the light armor materials program*. No. UCRL--51269. California Univ., 1972.

[130] Fukutomi, Hiroshi, et al. "Mechanism of texture formation during dynamic recrystallization of Ti-49 mol% Al." *materials transactions, jim* 35.11 (1994): 794-799.

[131] Hogan, James D., et al. "The effects of microstructure and confinement on the compressive fragmentation of an advanced ceramic." *Journal of the American Ceramic Society* 98.3 (2015): 902-912.

[132] Forquin, Pascal, et al. "Effect of aluminum reinforcement on the dynamic fragmentation of SiC ceramics." *International journal of impact engineering* 28.10 (2003): 1061-1076.

[133] Huy, Tran Duc, et al. "Microstructure and Mechanical Properties of TiAl3/Al2O3 in situ Composite by Combustion Process." *Materials Transactions* 55.7 (2014): 1091-1093.

[134] Boyce, Brad L., and Thomas B. Crenshaw. "Servohydraulic methods for mechanical testing in the sub-Hopkinson rate regime up to strain rates of 500 1/s." *Sandia National Laboratories Report, SAND2005-5678* (2005): 1-16.

[135] Mallick, D. D., et al. "A Simple Dual-Beam Time-Multiplexed Photon Doppler Velocimeter for Pressure-Shear Plate Impact Experiments." *Experimental Mechanics* 59.1 (2019): 41-49.